Version of Record: https://www.sciencedirect.com/science/article/pii/S0016706121004602
Manuscript_651242164175e3ba5ed7bffe2d7e47ce

Field-scale Estimation of Soil Properties from Spectral Induced Polarization Tomography

A. Revil[1], M. Schmutz[2], F. Abdulsamad[3], A. Balde[2,4], C. Beck [5],

A. Ghorbani[6], and S. S. Hubbard[4]

(1) Univ. Grenoble Alpes, Univ. Savoie Mont-Blanc, CNRS, UMR CNRS 5204, EDYTEM, 73370 Le Bourget du Lac, France
(2) Bordeaux INP – Université Bordeaux Montaigne, EA4592 Géoressources et Environnement, Talence, France
(3) Univ. Savoie Mont-Blanc, CNRS, UMR CNRS 5271, LOCIE, 73370 Le Bourget du Lac, France
(4) Lawrence Berkeley National Laboratory, Earth & Environmental Sciences, CA 94720, USA
(5) Université Grenoble Alpes, CNRS, IRD, IFSTTAR, ISTerre, 38000 Grenoble, France
(6) Yazd University, Department of Mining and Metallurgical Engineering, Yazd, Iran.

Corresponding author: André Revil andre.revil@univ-smb.fr

Emails: myriam.schmutz@ipb.fr; andre.revil@univ-smb.fr; feras.abdulsamad@univ-smb.fr; abdoulaye.balde@ipb.fr; sshubbard@lbl.gov; christian.beck@univ-smb.fr; ah.ghorbani@yahoo.fr

Highlights: (1) Laboratory investigations were used to refine a petrophysical model that links induced polarization properties to soil characteristics. (2) We image the spatial distribution of soil water content, CEC, mean grain size and permeability i. (3) Induced polarization is now mature enough to be used in agriculture and to study the critical zone.

Intended for publication in *GEODERMA*

© 2021 published by Elsevier. This manuscript is made available under the Elsevier user license
https://www.elsevier.com/open-access/userlicense/1.0/

Abstract. Estimates of soil properties such as Cation Exchange Capacity (CEC), water content, grain size characteristics, and permeability are important in geotechnical engineering, water resources, and agriculture. We develop a non-intrusive approach to estimate these properties in the field using spectral induced polarization (SIP) tomography. This geophysical method provides information about the frequency dependence of the complex electrical conductivity of porous media. Using 18 soil samples collected from a Bordeaux vineyard, we first conducted a laboratory study using SIP over the frequency range 10 mHz-45 kHz. The laboratory data were used to confirm the accuracy of a recently developed dynamic Stern layer petrophysical model. The results are consistent with published values from previous works using soils. A comparison was made by comparing the field complex conductivity spectra and the experimental data at two locations where core samples were obtained. The model was then used in concert with field data to image the spatial distribution of CEC, water content, permeability, and mean grain size along a vineyard transect. For clay and sandy textures found in the field, measured and estimated CEC agree rather well (from 6 to 40% discrepancy). Our approach provides an efficient way to estimate important soil properties in a non-invasive manner, in high resolution, and over field-relevant scales of the critical zone of the Earth.

Keywords: Induced polarization; chargeability, soil; grain size, cation exchange capacity, water content, tomography, critical zone.

1. Introduction

Soils are an essential component for supporting life on Earth. Currently, climate change and land-use change (including mechanical, chemical, and biological disturbances) are significantly reshaping soil systems (e.g., Acclimaterra Report, 2018). One of the main challenges of the coming decades is to combine protection of this finite soil resource (IPCC Special Report on Climate Change and Land, 2019) and its use in relation with the important context of growth of the world population. Optimal protection and management of soil properties for soil conservation (Dumanski and Peiretti, 2013), geotechnical engineering of the critical zone (Arthur, 2017), water resources (Arya et al., 1981; Ghanbarian et al., 2017), and agriculture (Sainju and Singh, 1997; Oliver et al., 2013) require accurate information about soil properties over field-relevant scales including soil grain size, permeability, cation exchange capacity (CEC), and water content.

Soil particle size distribution is an important soil property as it controls soil texture (e.g., Yolcubal et al., 2004), which is in turm essential regarding soil management. The connection between soil texture and plant competition is well-known in agricultural/viticultural soil management (e.g., van Leeuwen, 2010; Oliver et al. 2013) as well as in ecology of species management (e.g., Pennington et al., 2017; Eckhart et al., 2017). The clay, silt, sand or gravel fraction of soil texture also influence the permeability, a key parameter needed for groundwater flow and transport modeling (Lambe, 1955; Ikard et al., 2014, Hubbard, 2010). Granulometry can be estimated in the laboratory through several methods including sieving/sedimentation approaches. For instance, the French official standard NF X 31-107 involves five particle size classes defining soils categories (clay, silt, fine sand, coarse sand, coarse elements). More advanced methods include laser measurements (NF ISO 13320-1) combined with X-ray methods (i.e., Cnudde and Boone, 2013). Laser granulometry is a characterization technique based on light diffraction. The laser

granulometry allows a continuous grain size distribution between 0.63 and 2000 microns (10 values per decade), relative to sieving/sedimentation method.

Cation exchange capacity (CEC) is an important soil physico-chemical property. It represents the total capacity of soils to retain cations on soil particles at a given soil pH. CEC is mainly related to the content and type of clay and organic matter (Parfitt et al., 1995). It influences nutrient availability and characterize the reaction of soils to fertilizers (Hazleton and Murphy 2007). Water content can be locally determined with different probes such as neutron probes, capacitive sensors, and Time Domain Reflectometry (TDR) (e.g., Gardner, 1986, Topp, 2003). 'While soil sampling for water content determination is precise, it is destructive, time consuming, and often expensive to carry out using the sampling density required to capture natural soil variability (e.g., Gebbers and Adamchuk, 2010).

In recent decades, geophysical methods have been increasingly used for estimating soil texture for environmental and agricultural purposes (e.g., Rubin and Hubbard, 2005; Muzzamal et al., 2018). A variety of non-intrusive methods have also been increasingly used to characterize soil moisture, e.g., Ground Penetrating Radar (GPR) (e.g., Huisman et al., 2003), electromagnetic induction mapping (EIM) of resistivity (e.g., Altdorff et al., 2017; Zare et al., 2020), galvanometric electrical resistivity tomography (ERT, e.g., Friedman, 2005; Shah and Singh, 2005; Brunet et al., 2010), and nuclear magnetic resonance (NMR, Legchenko et al., 2002). Petersen et al. (2005) and André et al. (2012) demonstrated the relevance of geoelectrical methods for the characterization of the distribution of the different soil types, their moisture and CEC (Grote et al., 2010; Li et al., 2018; Martinez et al., 2018; Zare et al., 2020; Zhao, et al., 2020a, b).

Each of these geophysical methods has however intrinsic limitations. For instance GPR cannot be used in presence of conductive materials such as clayey soils. In order to reduce these intrinsic limitations, a combination of methods between geophysical and hard

data can represent an efficient approach (e.g., Robinet et al., 2018). While ERT has been widely used to estimate field-scale soil moisture, it is important to recognize that the assumptions used in published works may limit their applications. Electrical conductivity depends on two contributions, bulk and surface conductivities, both characterized by distinct dependence on the water content (Vinegar and Waxman, 1984, Revil et al., 1998). Surface conductivity has been often neglected without justification.

Here, we explore the value of Spectral Induced Polarization (SIP) method for estimating soil properties allowing to reinterpret field conductivity data without the need to neglect surface conductivity. With SIP, both electrical conductivity and (low-frequency) polarization are investigated over a range of frequencies. Polarization refers here to the reversible storage of electrical charges in a soil submitted to an applied electrical current. By low-frequency polarization, we mean polarization mechanisms occurring in the frequency range ~1 mHz-10 kHz.

The polarization mechanisms are operating at the grain or pore scales and are associated with the electrical double layer coating the grains (see Revil et al., 2017a, for soils). The existence of such polarization mechanisms is responsible for a phase lag between the electrical current and the electrical field (Olhoeft, 1981). These polarization mechanisms are different in nature from the dielectric polarization involved at higher frequencies (> 1 MHz) and their study was initially pioneered in the realm of colloidal chemistry (e.g., Dukhin and Shilov, 1974; Fixman, 1980).

Due to several recent key advances, the time has come to explore the value of SIP tomography for field-scale estimation of soil physiochemical properties in soil sciences. One of these developments is related to the existence of precise laboratory and field equipment. In SIP, in addition to measure an amplitude (resistance or conductance), we measure the phase lag between the current and the voltage. Accurate measurements of small phase angles below

1 mrad are now possible (e.g., Zimmermann et al., 2008; Kemna et al., 2012; Revil et al., 2012; Schmutz et al., 2014). Another key step forward has been the development of a fundamental polarization theory called the dynamic Stern layer model, that describes the underlying physics of SIP of soils (Revil et al., 2017a and references therein).

The paper is divided into three main sections. We first summarize the background theory. Then, we present a laboratory investigation regarding the relationships between the soil texture, permeability, and CEC and SIP data. Finally, we show how the SIP method can be applied in the field to image soil properties.

2. Polarization model based on the dynamic Stern layer

The complex conductivity σ^* of a soil can be characterized by its amplitude and phase lag between a sinusoidal current injected between two electrodes A and B and the potential difference measured between voltage electrodes M and N. The amplitude $|\sigma|$ (in S/m) and phase φ (in rad) can be recast into a complex-valued conductivity $\sigma^*(\omega)$:

$$\sigma^*(\omega) = |\sigma| e^{i\varphi} = \sigma'(\omega) + i\sigma''(\omega), \quad (1)$$

where $i^2 = -1$, σ' denotes the in-phase component (S m^{-1}, associated with conduction), σ'' (S/m^{-1}, associated with polarization) the quadrature conductivity (e.g., Olhoeft, 1981; Kemna et al., 2012), and $\omega = 2\pi f$ is the pulsation frequency. The polarization of a soil is associated with the ion accumulations at the grain scale because of the existence of the electrical double layer around the grains (Figure 1). The Stern layer is the layer coating directly the grains and formed by counterions defined as ions of opposite charge to the charge of the mineral surface.

The in-phase conductivity depends on two contributions corresponding to the bulk and surface conductivities. At a given pulsation frequency ω (expressed in rad s^{-1}) the in-phase conductivity can be expressed by (Vinegar and Waxman. 1984):

148 $$\sigma'(\omega) = \frac{1}{F} s_w{}^n \sigma_w + \sigma_S(s_w, \omega), \quad (2)$$

149 where σ_w (S m^{-1}) denotes the pore solution conductivity (temperature and salinity dependent),
150 , s_w (dimensionless) denotes the pore water saturation (s_w = 1 corresponds to full saturation, θ
151 = s_w, ϕ denotes the dimensionless volumetric water content, ϕ, dimensionless, denotes the
152 connected porosity of the soil), F the formation factor (dimensionless) connected to porosity
153 by $F = \phi^m$ (Archie's law, Archie, 1942), and σ_S (S m^{-1}) denotes the surface conductivity,
154 which depends on both saturation and frequency. The exponent m (dimensionless) is called
155 the first Archie exponent, the cementation exponent, or the porosity exponent. The exponent n
156 (dimensionless) denotes the second Archie exponent also called the saturation exponent.
157 Usually, we consider that $n \approx m$ (Revil et al., 2013b).

158 Values of the surface conductivity σ_S (in S/m) range between two limits, σ_S^0 (Direct
159 Current, DC, surface conductivity at low frequencies) and σ_S^∞ (a high-frequency asymptotic
160 value called the instantaneous surface conductivity). The frequency dependence of surface
161 conductivity is however weak (less than 10%). Low and high frequencies are defined with
162 respect to the distribution of the relaxation times characterizing the materials. These
163 relaxation times are themselves related to the distribution of characteristic length scales of the
164 porous material (typically pore or grain sizes).

165 In order to interpret complex conductivity spectra in a metal-free partially-saturated
166 porous material, a model called the dynamic Stern layer model is required (e.g., Revil, 2013a,
167 b, Revil et al., 2017a, Figure 1). Other low-frequency polarization mechanisms may exist such
168 as membrane polarization and metallic particle polarization mechanisms (Titov et al., 2002;
169 Revil et al., 2015a), but they are not consider to be relevant in our situation. When an
170 harmonic electric field $\mathbf{E} = \mathbf{E}_0 \exp(+i\omega t)$ (t refers to time) is applied to a porous material, its
171 complex conductivity is written as (Revil et al., 2017a)

$$\sigma^*(\omega) = \sigma_\infty - M_n \int_0^\infty \frac{h(\tau)}{1+(i\omega\tau)^{1/2}} d\tau \,. \quad (3)$$

where τ is a relaxation time (in s), and $h(\tau)$ denotes a (normalized) probability density for the relaxation times of the soil. The real-valued quantity σ_∞ (S m^{-1}) corresponds to the instantaneous conductivity of the soil while the real-valued term σ_0 (S m^{-1}) corresponds to its DC (Direct Current) conductivity (Figure 1). Their expressions are further described below. The normalized chargeability M_n corresponds to the difference between the instantaneous conductivity and the DC conductivity $M_n \equiv \sigma_\infty - \sigma_0$. Note that if the chargeability is determined between two intermediate frequencies f_1 and f_2 (i.e., $M_n(f_1, f_2) = \sigma'(f_2) - \sigma'(f_1)$, $f_2 > f_1$ it is necessarily smaller than the integrated normalized chargeability $M_n \equiv \sigma_\infty - \sigma_0$ because the conductivity monotonically increases with the frequency.

Equation (3) is general. When the polarization length scales obey a log normal distribution, the complex conductivity can be expressed by a Cole Cole model

$$\sigma^* \approx \sigma_\infty \left(1 - \frac{M}{1+(i\omega\tau)^c}\right), \quad (4)$$

where c denotes the Cole Cole exponent, which describes the broadness of the density probability distribution of the relaxation times, and $M = M_n / \sigma_\infty$ (dimensionless) denotes the chargeability. If the core samples are characterized by a bi-modal grain size distribution, we can consider that the complex conductivity is given by a double Cole Cole model In this paper, we will use such double Cole Cole model (Appendix A) to determine Cole Cole parameters for a collection of 18 soil core samples from the test site. Sometimes the soil samples can be characterized by very flat spectra (e.g., Vinegar and Waxman, 1984; Revil et al., 2017a) and in this case, it is not possible to estimate the Cole Cole parameters, and the spectra are better described by a constant phase model.

When a soil is partially saturated with a pore water electrolyte and assuming that $m \approx n$, Revil (2013a, b) obtained the following relationships:

$$\sigma_\infty = \theta^n \sigma_w + \theta^{n-1} \rho_g B \mathrm{CEC}, \tag{5}$$

$$\sigma_0 = \theta^n \sigma_w + \theta^{n-1} \rho_g (B - \lambda) \mathrm{CEC}, \tag{6}$$

$$M_n = \theta^{n-1} \rho_g \lambda \mathrm{CEC}, \tag{7}$$

where equation (7) results from equations (5) and (6), ρ_g denotes the grain density (in kg m^{-3}), and CEC denotes the cation exchange capacity of the soil expressed in C kg^{-1} or in meq/100 g (1 meq/100 g = 963.20 C kg^{-1} in SI units), B (in $m^2 s^{-1} V^{-1}$) denotes the apparent mobility of the counterions for surface conduction (associated with the in-phase conductivity) and λ (in $m^2 s^{-1} V^{-1}$) denotes the apparent mobility of the counterions for the polarization associated with the quadrature conductivity (see Vinegar and Waxman, 1984). From equations (5) to (7), when the bulk water conductivity dominates the conductivity, the phase is inversely proportional to the saturation.i

A dimensionless number R was introduced by Revil et al. (2017a, b, c) as $R = \lambda / B$. The two surface conductivities mentioned above are given explicitly as $\sigma_S^0 = \theta^{n-1} \rho_g (B - \lambda) \mathrm{CEC}$ and $\sigma_S^\infty = \theta^{n-1} \rho_g B \mathrm{CEC}$. From Ghorbani et al. (2018), we have $B(Na^+, 25°C) = 3.1 \pm 0.3 \times 10^{-9}$ $m^2 s^{-1} V^{-1}$ and $\lambda(Na^+, 25°C) = 3.0 \pm 0.7 \times 10^{-10}$ $m^2 s^{-1} V^{-1}$, and $R \approx 0.10 \pm 0.02$.

Considering the quadrature conductivity at the geometric mean frequency of two frequencies f_1 and f_2 and the normalized chargeability defined as the difference between the in-phase conductivity at the frequency f_2(> f_1) and the in-phase conductivity at the lower frequency f_1, we can connect the quadrature conductivity and the normalized chargeability with (Van Voorhis et al., 1973; Revil et al., 2017a)

$$\sigma''\left(\sqrt{f_1 f_2}\right) \approx -\frac{M_n(f_1, f_2)}{\alpha}, \tag{8}$$

$$\alpha \approx \frac{2}{\pi} \ln A , \tag{9}$$

and A denotes the number of decades between f_1 and f_2 (for 3 decades, we have $A = 10^3$ and $\alpha \approx 4.4$). Equations (7) and (8) provide the relationship between the quadrature conductivity and the CEC. Equations (8) and (9) are not related to the dynamic Stern layer model and can be derived from the constant phase model. That said, as noticed in Revil et al. (2017a), there are very accurate for soils characterized by broad distribution of the relaxation times. From equation (8) and the expression of the surface conductivity, we can draw a relationship between the quadrature conductivity and the surface conductivity σ_S^{∞} as

$$-\frac{\sigma''\left(\sqrt{f_1 f_2}\right)}{\sigma_S^{\infty}} = \frac{M_n(f_1, f_2)}{\alpha \sigma_S^{\infty}} = \frac{R}{\alpha}. \tag{10}$$

Since R and α are both two constants (independent of frequency, temperature, and saturation), this means that the quadrature conductivity and the surface conductivity are proportional to each other. Equation (10) is exact for the constant phase model, which is characterized by the absence of peaks in the quadrature conductivity spectra.

The last parameter to discuss in terms of soil property characterization is the Cole Cole relaxation time τ. According to Revil et al. (2012), we have:

$$\tau = \frac{d^2}{4m^2 D_{(+)}} \theta^2 , \tag{11}$$

where $D_{(+)}$ denotes the diffusion coefficient of the counterions in the Stern layer (in $m^2 s^{-1}$). The value of this diffusion coefficient $D_{(+)}$ is connected to the mobility of the counterions, B, by the Einstein relationship $D_{(+)} = k_b T B / e$, where e is the elementary charge, T denotes the absolute temperature (in K), and k_b denotes the Boltzmann constant (1.3806×10^{-23} m^2 kg s^{-2} K^{-1}). At saturation, Equation (11) reduces approximately to $\tau \approx d^2 \phi^2 / 16 D_{(+)}$ with $m \approx 2$. With

240 equation (11) and equations (4) to (7), we can predict the effect of saturation on the shape of
241 the spectra.

242 # 3. Laboratory investigations

243 ## 3.1. Soil sample Analysis

244 18 soil disturbed samples were extracted with a hand auger along a 47 m transect in a
245 vineyard located near Bordeaux (Léognan, Gironde, France). Soils along the transect are
246 dominated by colluviosol (Baize and Girard, 1998). The samples were acquired from horizons
247 H1 and H2 (see Figure 2) A total of 18 samples were extracted with a hand auger from the test
248 site along the profile and at depths ranging between 0.2 to 1 m (Tregoat (2007). The samples
249 were associated with the pedologic horizons H1, H2, and H3. Soil samples E1, E4, E5, E7,
250 E8, E9, E12 and E17 belong to Horizon H1 (from 0 to 0.4 m). These soils are classified as
251 sands in the GEPPA soil classification, having gravel content up to 20%, silt content up to
252 25% and clay content up to 7%. Core samples E2, E6, E10, E13, E18, E11, E14 and E19
253 belong to Horizon H2 (from 0.4 to 1 m). These samples are also classified as sand (with some
254 gravels up to 15%). The core samples E3 and E15 were extracted at a depth of 1 m at the
255 interface between Horizons H2 and H3. H2 is indicated as redoxic. The clay content in H2
256 may reach 12% and the silt fraction may range from 0 to 25%. The horizons H1, H2, and H3
257 are characterized by the presence of organic matter (0.7% in H1, 0.13% in H2, and 0.57% in
258 H3). Note that the presence of the organic matter can influence the CEC of the soil (Parfitt et
259 al., 2008). The swelling character of the soil may indicate the presence of smectite. Typical
260 grain size distribution are shon in Figure 3.

261 Additionally, a core was extracted on the profile at a depth of 3.3 m depth indicating
262 that there is no water table at least until a depth of 3 m . This core sample demonstrates the
263 existence of a compact clay layer below 1.5 m. This clay layer represents the non-calcareous
264 residue of the underlying limestones. Its existence and composition is of major importance for

265 explaining the properties of soils in the test site. Under the temperate climate of France, this
266 clay layer is rich in swelling clays like smectite (Platel et al., 2004)

267 The granulometry of each sample was determined with a MALVERN Sizer 2000 laser
268 granulometer. The sample texture is defined according to the soil texture classification of
269 GEPPA (Groupe d'Etudes des Problèmes de Pédologie Appliquée, 1963). The dark colour of
270 the shallow samples (0-0.3 m) suggests that they contain organic matter. The porosity of the
271 soil samples was estimated with weight and volume measurements. The cation exchange
272 capacity was obtained with the cobalthexamine titration method (Aran et al. 2008).

273 The pH_{H20} and pH_{KCl} measurements are done according to the NF ISO 10390 norm,
274 which specifies a method for pH measurement using a glass electrode in a suspension of soil
275 diluted 1:5 (vol. fraction) in water and in a solution of KCl at 1 mol / l (pH of KCl) or in a
276 solution of calcium chloride at 0.01 mol L^{-1}. The OM measurements were performed
277 according to the NF ISO 14235 norm by sulfochromic oxidation This international standard
278 specifies a method for the spectrometric determination of the organic carbon content in soil
279 after oxidation in a sulfochromic medium. The properties of the core samples are summarized
280 in Tables 1 and 2.

281 **3.2. Laboratory SIP measurements**

282 Frequency-domain induced polarization measurements were performed over the
283 frequency range 10 mHz-45 kHz using the ZELSIP04-V02 impedance meter (Zimmermann et
284 al., 2008). We use the same experimental protocol and sample holder as in Revil et al. (2017a,
285 see Figure 4). Non-polarizable Ag/AgCl medical electrodes were used both for the current
286 injection (electrodes A and B) and potential electrodes M and N. Some spectra are shown in
287 Figure 5 together with the equivalent circuit model that will be used to interpret them
288 according to the theory described in Section 2. The spectra are fitted with the double Cole

289 Cole model described in Appendix A and the Cole Cole parameters are reported in Table 2. A
290 fit of the spectra is shown in Figure 6.

291 **3.3. Influence of the pore water salinity**

292 The spectral response was measured for the 18 (disturbed) soil samples fully saturated
293 at 3 salinities (NaCl solutions) corresponding to the following values of the electrical
294 conductivity σ_w = 0.0720, 0.56, and 6.22 S m^{-1} (at 25°C) using protocol developed in Revil et
295 al. (2017a). Just for completeness, we first washed the core samples, which are then saturated
296 under vacuum with a degassed NaCl solution of determined salinity. Then the samples are
297 stored one month to equilibrate with their solution. The volume of solution is such that the
298 cation exchange between the pore water and the surface of the grains will not impact the
299 conductivity of the solution. The reported conductivity is anyway the conductivity of the
300 solution measured right before prior performing the SIP spectra. Then for the two other
301 salinities, the change of pore water solutions is done by diffusion with the samples in contact
302 with a new NaCl brine to avoid desaturation of the core samples.

303 The dependence of the in-phase conductivity with the pore water conductivity (Figure
304 7) was used to invert the value of the formation factor F and surface conductivity σ_S by fitting
305 the data with equation (2) for each core sample. Then, for each sample, the cementation
306 exponent was determined from m = -log F / log θ_S. Figure 7 shows that for low pore water
307 salinities (typically below 10^{-2} Mol L^{-1} equivalent NaCl), the (in-phase) conductivity of soils
308 is dominated by the surface conductivity because of the presence of the electrical double layer
309 surrounding the grains. The values of the formation factors and surface conductivity (at 1
310 Hertz) are reported in Table 1.

311 **3.4. Petrophysical relationships**

In Figure 8, the formation factor versus the (connected) porosity is plotted. The data set is fitted with an Archie's law $F = \phi^{-m}$. For the samples, a typical value of the cementation exponent is about $m \approx 1.71 \pm 0.10$. Then, we explore the relationship between the quadrature conductivity and the surface conductivity. Both the quadrature and surface conductivity are related to the electrical double layer and, according to the dynamic Stern layer model, their ratio is a constant. This linear relationship is confirmed by the trend shown in Figure 9. We then explore the relationship between the normalized chargeability (between 1 Hertz and 1 kHz) and the quadrature conductivity at the geometric frequency of 32 Hertz (see equations 11 and 12). As shown in Figure 10, this linear relationship is also confirmed by the experimental data. The slopes of the trends show in Figures 9 and 10 can be used to estimate the value of the mobilities B and λ.

3.5. Effect of the cation exchange capacity

Figures 11, 12, 13, and 14 show that the samples used in this study are consistent with other datasets made on porous rocks. Surface and quadrature conductivities are linearly related to the cation exchange capacity of the material (surface conductivity refers here to the instaneous surface conductivity, which is close to the DC surface conductivity). The dependence of the quadrature conductivity with the CEC is derived by combining equations (7) and (8). The effect of the tortuosity of the bulk pore space is shown in Figure 13 for a set of core samples with a broad range of porosity.

3.6 The relaxation time

In Figure 15, we test the relationship $\tau = d^2\phi^2 / 16 D_{(+)}$ derived from equation (11) We get a fair agreement between the model and the data with $D_{(+)} = (2.5 \pm 0.5) \times 10^{-9}$ m^2 s^{-1}. Given that most of the core sample are sandy soils, at low frequencies (below 100 Hertz) the relaxation τ_1 primarily reflects the sand grains (Appendix A), which is much slower in

principle than the relaxation of the clay particles (relaxation 2, see Appendix A). The diffusion coefficient of sodium in water is close to $D_{(+)}$ ~1.5×10^{-9} m^2 s^{-1}, a value close to the previous estimate ($D_{(+)}$ = $(2.5\pm0.5)\times10^{-9}$ m^2 s^{-1}). Note that the Stern layer of pure silica is weak as discussed extensively in Revil (2014). In principle, the determination of the relaxation time can be useful for estimating the mean grain sizes of the coarse fraction of the core sample. For clay minerals, using d = 2 μm for clay, ϕ = 0.40 (Table 1), τ = $2\text{x}10^{-5}$ s (Table 2) in $D_{(+)} \approx d^2\phi^2 / 16\tau_2$ yields 2×10^{-9} m^2 s^{-1}.

4. Field application

4.1. Data acquisition

A 47.25 m-long SIP profile was acquired in the vineyard (Figure 3) June, 26 in the morning in 2017. Measurements were done after a moderate rain this day, that followed a very dry period: the cumulative curve indicates 30mm rain since June 1.

We used 64 electrodes with a spacing of 0.75 m. SIP data were acquired using an eight-channel field impedance meter DAS-1 system from Multi-Phase Technologies (MPT, http://www.mpt3d.com/das1.html). This system is based on a 24-bit A to D converter and microprocessor. In the spectral IP operating mode, the system was operated at 14 frequencies (0.125, 0.25, 0.5, 1, 1.5, 2.5, 5, 7.5, 12, 25, 37.5, 75, 112, and 225 Hz), covering therefore three orders of magnitudes. Two stacks were performed. We used a pseudo-Wenner sequence (144 measurements) and two cables, one for the current electrodes AB and one for the voltage electrodes MN (Figure 16). The voltage electrodes MN were non-polarizable electrodes while the current electrodes AB were stainless steel electrodes. The contact resistances between the electrodes and the ground was always below 3 kΩ, an acceptable value according to our experience in operating field measurements. The cables were placed approximately 40 cm above the ground to reduce capacitive coupling effects. The acquisition took 3 hours.

362
363 **4.2. Dataset and tomography**

364 We first plot the pseudo-sections of the SIP imaging data set independently for each
365 frequency. We filtered the 5 Hz component of the dataset because of an issue with the DAS
366 equipment, and filtered or suppressed other outliers that may have occurred. If the outlier
367 occurs between neighbors on the phase-shift versus frequency diagram, this data point is
368 removed out of the dataset. The phase-shift of the electrical impedance measurements
369 generally revealed quite smooth variations in the pseudo-section in the frequency range 0.125
370 Hz-37.5 Hz. The phase ranged from 0.7 mrad to 10.6 mrad at 0.125 Hz, and from 0 ± 2mrad
371 to 20 mrad at 37.5 Hz. No filtering was necessary between 0.125 to 7.5Hz. Some isolated
372 outliers between for 12, 25Hz had been removed, and severe filtering would have been
373 necessary up to 37.5Hz. Up to 37.5Hz and especially up to 75Hz, many inconsistent phase-
374 shifts occurred related to unwanted electromagnetic (EM) inductive and capacitive effects
375 (Ghorbani et al., 2009, Schmutz et al., 2014). Capacitive effects arise due to differences in the
376 contact resistances (i.e., between electrodes and the ground), or the conductive shields of the
377 cables and the surface (e.g., Zimmermann et al., 2008; Zhao et al., 2013). Inductive effects are
378 related to the current flow along the cables connecting the electrodes and the measuring
379 devices, and their magnitude is proportional to the cable length, the electrical conductivity of
380 the subsurface, and the frequency (e.g., Schmutz et al., 2014; Flores Orozco et al., 2018). The
381 pseudo-Wenner sequence provided very clean data. We did not have to perform any filtering
382 at all for the conductivity data. ~~Regarding the phase, no data were filtered out in the frequency~~
383 ~~band 0.125Hz – 2.5Hz, 5 data were removed at 7.5Hz, and 10 data were removed at 25 Hz.~~
384 We focus only on the first 4 m of the section for which the depth of investigation (DOI) can
385 be determined. .

386 Each frequency of the whole data set was independently inverted with the code
387 IP4DI_2D (Karaoulis et al., 2013). The (Root Mean Square Error) RMSE is in the range 2 to

388 5% (5% at 25Hz) depending on the frequency. A finite difference mesh was created and the
389 covariance matrix was calculated taking into account the standard deviation of measurements.
390 We used a Levenberg-Marquardt inversion algorithm and the Jacobian matrix was updated at
391 each iteration. An insulating boundary condition is used at the ground surface since the
392 normal component of the current density vanishes at the ground surface. The mesh is built in
393 order to insure that the other boundaries mimic infinity boundary conditions for which the
394 potential is equal to zero. The inversion converged at the 5th iteration for all the frequencies.
395 Once each frequency had been inverted, for each position, we developed a complex
396 conductivity spectrum over the frequency range 0.125 to 37.5 Hz. Figure 17 shows the
397 resulting amplitude of the conductivity and the phase at 1 Hertz and Figure 18 shows the in-
398 phase conductivity and quadrature conductivity tomograms at the same frequency.

399 In order to test equations (8) and (9) on the field data, we represent the partial
400 normalized chargeability (determined as the difference between the in-phase conductivity at
401 25 Hertz and 0.25 Hertz) versus the quadrature conductivity σ'' determined at the geometric
402 mean of 2.5 Hertz, as shown in Figure 19. According to equation (9), the slope α should be
403 2.9. The field data exhibit a linear trend fairly consistent with this prediction with a slope
404 close to 2.9.

405 In Figure 20, we compare the field data to the laboratory data at the position of the
406 core samples E15 and E19. The observed shift between the field and laboratory data is likely
407 due to a difference in the saturation between the laboratory experiments and the in situ
408 conditions. Figures 20c and 20d, we observe a very good correspondence between the field
409 and laboratory data in terms of dependence with the frequency. We can conclude from
410 Figures 19 and 20 that the field data quality is sufficiently good and proceed with estimation
411 of soil properties, as is described in the next section.

412 **4.3. A strategy to estimate soil properties**

Using the conductivity and phase data and equation (1), we obtain the tomograms for the in-phase and quadrature conductivities. From the quadrature conductivity, we can image the normalized chargeability $M_n = -\alpha\sigma''$ with α = 9 to include the total normalized chargeability accounting for the full range of relaxation times. Then, using equations (5) and (7) and solving a two observations (conductivity/normalized chargeability)/2 unknowns (water content, CEC) problem, we obtain:

$$\theta = \left[\frac{1}{\sigma_w} \left(\sigma_\infty - \frac{M_n}{R} \right) \right]^{1/m}, \tag{12}$$

$$\mathrm{CEC} = \frac{M_n}{\theta^{m-1} \rho_g \lambda} \cdot \tag{13}$$

From equation (12) and (13), we estimate the water content and the CEC distributions using the conductivity and normalized chargeability tomograms. Consistent with our laboratory experiments on sandy samples, we use the following parameters for equations (12) and (13): m = 1.71 (Figure 8), ρ_g = 2800 kg m^{-3} (average values measured on the core samples), λ (15°C) =3.0±0.7×10^{-10} m^{-2}s^{-1}V^{-1}, R = 0.12, and σ_w(15°C) = 0.4 S m^{-1} representing the brackish water influenced by the use of fertilizers at the site. The days before the field measurements, fertilizers were indeed amended, and this was a period of heavy fertilizing because of heat/moisture that might lead to grape illness. Also, it was a dry month (30 mm cumulative rainfall between June 1st and June 26th day) even if the day of the measurement a moderate rain occurred before the measurements (a heavy rain occurred just after the measurements). The quantities m, ρ_g, R are saturation and temperature independent.

Figure 21 shows the tomogram of CEC and water content θ estimated using the field data and equations (14) and (15). High CEC (>15 meq/100 g) values are consistent with swelling clay with a high percentage of vermiculite possibly as high as 20%, which is classical of a clay layer resulting from the weathering of the underlying calcareous bedrock. Induced polarization can be used to estimate permeability at full or partial water saturation

(for instance Revil et al., 2015b). The soil permeability k (m^2) is estimated from the cation exchange capacity CEC (in C kg^{-1}) and the formation factor F according to $k = k_0(1/FQ_V)^c$ (Sen et al., 1990) where k_0 and c are two fitting parameters, $F = \phi^{-m}$ and $Q_V = \rho_g(1-\phi)\mathrm{CEC}/\phi$. This equation was validated silicoclastic geological media. According to Soueid Ahmed et al. (2020), this equation can be generalized to unsaturated conditions:

$$k \approx \frac{10^{4.3}\theta^6}{\left(\rho_g \mathrm{CEC}\right)^2}. \quad (14)$$

Using Equation (14) with estimates from spectral induced polarization tomography for the water content and CEC, we image the soil permeability (Figure 22). This figure reveals that the middle layer is quite impermeable (<< 1.10^{-15} m²) and may act locally as a seal.

The last step is to use the relaxation time to estimate the spatial distribution of soil mean grain size. We use the formula adapted to unsaturated conditions (see equation 11) to relate the mean grain size to the water content,

$$d = \sqrt{\frac{16 D_{(+)} \tau(\theta)}{\theta^2}}, \quad (15)$$

using m = 2. We apply equation (15) to each cell of the tomogram using the relaxation time inverted from the spectra and the water content from the tomogram shown in Figure 21.

At first, the agreement between the particle size fractions between the measured versus the predicted values is only fair. Obviously the support volume for the two dataset is different approximately 0.0002 m^3 for the core samples versus 0.6m^3 for the field data. That said, the main granulometric textures are well retrieved from the geophysical data with one core sample corresponding to clay (< 2μm), 3 core samples corresponding to silts (2-20 μm), and 15 core samples corresponding to fine sands (20 – 200 μm). The clay and silt fractions can only be detected thanks to the quadrature conductivity because of the frequency range used in the field. regarding the 15 core samples corresponding to fine sand according to the

460 geophysical data,, 12 core samples are effectively in the size range observed in the laboratory
461 (20-200 micrometers) and the 3 others are defined as coarser sands.

462 The application of equation (15) is, however, not used in areas defined by quadrature
463 conductivity > 3.5×10^{-4} S m^{-1} and in the range 2.4×10^{-4} to 3.5×10^{-4} S m^{-1} corresponding to
464 clayey and silty areas, respectively. The resulting tomogram is shown Figure 23. This figure
465 can be divided into 2 parts. The first part corresponds to the sandy soils with a subdivision
466 between fine sands and silts (20-200 μm), coarse sand (200-2000 μm), and coarse material
467 like pebbles (>2000 μm). In this part, the finest grain size (<80 μm) may not be defined if the
468 characteristic frequency occur outside of the used frequency range, or in case of uncertainty of
469 the frequency peak if data filtering/suppression should occur at the highest frequency (37.5
470 Hz) used in our study.

471 The second part of the figure corresponds to clay-silt material for which we assign the
472 value “20 μm” for silts and “2 μm” for clay, corresponding to the highest mean grain size for
473 clay and silt soil textures. We adopt this strategy as our field frequency range is restricted to a
474 narrow range. The results suggest the presence of sandy soils above and below a clay layer.
475 Also the obtained values are consistent with the values measured for the extracted samples,
476 and show an important heterogeneity of the soil texture classes. So, the relaxation times can
477 be used to infer an information regarding the grain sizes of the materials.

478 ## 5. Discussion

479 We first summarize the procedure used in this work. We used 5 steps to estimate the
480 material properties of interest in the field. (1) We inverted the in-phase and quadrature
481 conductivities for a range of frequencies. The quadrature conductivity was transformed into a
482 normalized chargeability for each cell used to discretize the subsurface. (2) For each cell, the
483 normalized chargeability and the in-phase conductivity are used to determine the water
484 content and the CEC. (3) For each cell, the water content and the CEC are used to infer the

485 permeability. (4) The relaxation times are inverted cell by cell regarding the spectra at the
486 corresponding cell. (5) At each cell, the water content and the relaxation times are used to
487 infer the mean grain size for this cell.

488 The CEC values inferred from the spectral induced polarization tomography data are
489 consistent with the range of values obtained in the laboratory (see Tables 3 and 4 for a
490 comparison). From our geophysical study, the CEC of the clay formation is found to be in the
491 range 25-55 meq/100 g (with a mean of 43 meq/100 g). This can be compared to the CEC of a
492 clay core samples taken inside the clay formation and characterized by a CEC in the range 40
493 meq/100 g (Table 4). In Figure 24, we compare the CEC determined from the geophysical
494 data and the CEC determined from the laboratory measurements. The values are averaged for
495 each texture (4 samples for texture SS, 8 samples for texture S1, 4 samples for textures Ls,
496 and 1 sample for each texture LL and AA). The geophysical data are able to predict the CEC
497 of the different textures (slope of 1.03, $r^2 = 0.93$).

498 The soil volumetric water content are globally low, in the range 9-25% close to the
499 surface. The shallow moisture values are consistent with TDR measurements ranging between
500 15 and 25 vol.% at a 8cm depth performed at the end of June consistently with the field
501 induced polarization measurements. During the field measurements, the weather was warm
502 (25-30°C) and the weather was dry (30mm cumulated precipitation for the last 3.5 weeks
503 before the field data acquisition). The water table is located at a depth of 3.5 m. The clay layer
504 is likely water-saturated because of its high capillary pressure. The low water content of this
505 layer means that its porosity is low because it is composed of a high density clay material.

506 The grain size tomography exhibits promising results since the derived grain sizes are
507 compatible with the ones expected from the samples analysis, pedology, and core drilling (see
508 Figure 15 and 23 and equation 15). The drilling attests that a strong swelling clay is also
509 present at deeper depths (between 1 and 3m). We can define 3 kind of categories of grain

510 sizes. The first two are composed of clay and silt zones. They are defined through their
511 imaginary part of the conductivity values. From the laboratory data, the clay zone is defined
512 by quadrature conductivities > 3.5×10^{-4} S m^{-1} while silt areas have quadrature conductivities
513 in the range 2.4×10^{-4} and 3.5×10^{-4} S m^{-1}. The third grain size category (nine samples)
514 corresponds to fine sands with grains size typically around 100-125 μm. For these samples,
515 the calculated main grain size retrieved from spectral induced polarization tomography are
516 comprised between 101 and 233 μm, with most values between 101 and 147 μm, except for
517 sample E15 and E13 which are ~189 and 233 μm instead of 125 μm (from laser
518 measurements). Note also that a significant fraction of coarse elements may be present (or
519 even be predominant in some areas). The relaxation frequency of these coarse elements is
520 very low (between 0.25 and 5 Hz) outside the range investigated in the present study. In the
521 future, and to get a broader grain size distribution from SIP tomography, the frequency range
522 in the field the use of lower and higher frequencies should be considered.

523 Finally, a fundamental question is to know if, in field conditions, surface conductivity
524 is negligible or not since in a large number of studies in hydrogeophysics, surface
525 conductivity is neglected without any discussion about this point. In Figure 25, we plot from
526 the field data at the position of the core sample the normalized chargeability (from the
527 inversion of the spectra) versus the instantaneous conductivity. The slope being close to R =
528 0.13 (Figure 25a), this indicates that for the field conditions, surface conductivity dominates
529 the conductivity response in the field (if this is not the case, the slope should be smaller than
530 R). In Figure 25b, we plot some of the laboratory data in which the conductivity of the core
531 samples is plotted as a function of the conductivity of the pore water. We add the range of
532 plausible pore water conductivities in the field conditions. We see clearly that surface
533 conductivity is extremely important in the overall conductivity response of these sandy soils.

534 Therefore the application of a conductivity equation neglecting surface conduction would be
535 erroneous.
536

537 ## 6. Conclusion

538 Spectral Induced Polarization (SIP) in the frequency range 0.25-25 Hertz is a powerful
539 geophysical method to image soil properties. We apply here the dynamic Stern layer model of
540 induced polarization of Revil et al. (2017a) to a new dataset of soils from a Bordeaux
541 vineyard. The experimental data are consistent with the dynamic Stern layer model and
542 theory. The analysis is performed for the surface conductivity, the quadrature conductivity
543 and normalized chargeability, and the main relaxation times using a Cole Cole complex
544 conductivity model. From these results, a strategy was developed to interpret field data. We
545 acquired field spectral induced polarization measurements in the frequency range 0.125 Hz to
546 75 Hz. The quality of the field data set was further checked by looking at the relationship
547 between the normalized chargeability (between 0.25 Hertz and 25 Hertz) and the quadrature
548 conductivity at 2.5 Hertz. Some comparisons were also made by comparing the field spectra
549 and the experimental data at 2 locations where core samples were extracted. Finally, the field
550 data were used to image the water content, the Cation Exchange Capacity, the mean grain
551 size, and the permeability down to a depth of 4 meters and validation stems from the first
552 meter of the subsurface. A shallow smectite-rich clay layer is identified and characterized.

553 To the best of our knowledge, this is the first field scale estimation of CEC, grain size,
554 water content, and permeability using spectral induced polarization tomography in soils. That
555 said, the quality of predictions need to further assessed in future studies embracing more
556 divers environments, soil use (e.g., including roots) and combined with soil measurements
557 The present study confirms also the applicability of the dynamic Stern layer model to
558 understand induced polarization of soils in terms of fundamental physicochemical parameters.

559 We have shown that surface conductivity cannot be neglected in the field. Spectral induced
560 polarization tomography can be now used for agricultural purpose and the study of the critical
561 zone and the method needs to be improved to higher frequencies. The present approach has
562 assumed that sodium was the main counterions in the Stern layer. The influence of
563 heterogeneity in the chemistry of the soil samples could be accounted for. In irrigated fields,
564 heterogeneous distribution of chemical species (especially in the vertical direction) can occur
565 and a more complex dynamic Stern layer model should be applied as shown by Vaudelet et al.
566 (2011a, b).
567
568 **Acknowledgements.** We thank the INTERREG SUDOE project "Soil Take Care" for
569 funding. and the Chateau "La Louviere" in France for access to their domain. The authors are
570 grateful to C. Arbogast for his help in the field. S. Hubbard was supported through the
571 Watershed Function Scientific Focus Area funded by the U.S. Department of Energy, Office
572 of Science, Office of Biological and Environmental Research under Award Number DE-
573 AC02-05CH11231. The data are provided in DRYAD
574 (https://doi.org/10.5061/dryad.n02v6wwvs). We thank the Editor, Dr. Cristine Morgan, and
575 three anonymous referees for their very useful comments.
576

References

Abdulsamad, F., Revil, A., Soueid Ahmed, A., Coperey, A., Karaoulis, M., Nicaise, S., Peyras, L., 2019. Induced polarization tomography applied to the detection and the monitoring of leaks in embankments. Engineering Geology 254, 89-101. https://doi.org/10.1016/j.enggeo.2019.04.001.

AcclimaTerra, Le Treut, H. (2018). Anticiper les changements climatiques en Nouvelle-Aquitaine. Pour agir dans les territoires. Éditions Région Nouvelle-Aquitaine, 488 pp.

Altdorff, D., von Hebel, C., Borchard, N., van der Kruk, J., Bogena, H.R., Vereecken, H. and Huisman, J.A. (2017). Potential of catchment-wide soil water content prediction using electromagnetic induction in a forest ecosystem. Environ Earth Sci. 76(111). https://doi.org/10.1007/s12665-016-6361-3.

André, F., Saussez, S., Moghadas, D., Van Durmen, R., Delvaux, B., Vereecken, H., Lambot, S., de Rességuier, L., Van Leeuwen, C., and Bogaert, P. (2012). High-Resolution Imaging of a Vineyard in South of France Using Ground-Penetrating Radar, Electromagnetic Induction and Electrical Resistivity Tomography. Journal of Applied Geophysics, 78, 113–22.

Aran, D., Maul, A., and Masfaraud, J.F. (2008). A spectrophotometric measurement of soil cation exchange capacity based on cobaltihexamine chloride absorbance. Comptes Rendus Geoscience, 340(12), 865–871. https://doi.org/10.1016/j.crte.2008.07.015.

Archie, G. E. (1942). The electrical resistivity log as an aid in determining some reservoir characteristics. SPE-942054-G, 146, 54–62. https://doi.org/10.2118/942054-G.

Arya, L.M. and Paris, J.F. (1981). A Physicoempirical Model to Predict the Soil Moisture Characteristic from Particle-Size Distribution and Bulk Density Data. Soil Science Society of America Journal, 45(6), 1023-1030. https://doi.org/10.2136/sssaj1981.03615995004500060004x.

602 Baize, D., and Girard, M. (1998). A Sound Reference Base for Soils: The "Référentiel
603 Pédologique". Institut National de La Recherche Agronomique, Paris, Editors.
604 Bolève, A., Crespy, A., Revil, A., Janod, F., and Mattiuzzo, J. L. (2007). Streaming potentials
605 of granular media: Influence of the Dukhin and Reynolds numbers. J. Geophys. Res. 112,
606 B08204. https://doi.org/10.1029/2006JB004673.
607 Börner, F. D. (1992). Complex conductivity measurements of reservoir properties,
608 Proceedings of the Third European Core Analysis Symposium, Paris, 359-386.
609 Brunet, P., Clément, R. and Bouvier C. (2010). Monitoring soil water content and deficit
610 using Electrical Resistivity Tomography (ERT) – A case study in the Cevennes area,
611 France. Journal of Hydrology, 380(1-2), 146-153.
612 https://doi.org/10.1016/j.jhydrol.2009.10.032
613 Churcher, R.L., French, P.R., Shaw, J.C., and Schramm, L.L. (1991). Paper SPE 21041
614 presented at the 1991 Int. Symp. On Oilfield Chemistry, Anaheim, February 20-22.
615 Cnudde, V., and Boone, M. N. (2013). High-resolution X-ray computed tomography in
616 geosciences: A review of the current technology and applications. Earth-Science
617 Reviews, 123, 1-17.
618 Comparon L. (2005). Etude expérimentale des propriétés électriques et diélectriques des
619 matériaux argileux consolidés. PhD Thesis, Institut de Physique du Globe de Paris 400
620 pp. https://hal.archives-ouvertes.fr/tel-00135855/.
621 Dukhin S.S., and Shilov V.N. (1974). Dielectrical phenomena and the double layer in disperse
622 systems and polyelectrolytes. Wiley, New York.
623 Dumanski, J., and Peiretti, R., (2013). Modern concepts of soil conservation International Soil
624 and Water Conservation Research 1(1), 19-23. https://doi.org/10.1016/S2095-
625 6339(15)30046-0.

626 Eckhart, V.M., , M.R., , K., , B.K., , D.M., , Y. and M.A. (2017). Contrasting soil-texture
627 niches facilitate coexistence of two congeneric plants that differ in competitive ability.
628 *AoB PLANTS*, 9(6), plx066. .
629 Fixman, M., (1980), Charged macromolecules in external fields. I. the sphere: Journal of
630 Chemical Physics, 72(9), 5177–5186, https://doi.org/10.1063/1.439753.
631 Flores Orozco, A., Bücker, M., Steiner, M., and Malet, J-P. (2018). Complex conductivity
632 imaging for the understanding of landslide architecture. Eng. Geology 243, 241-252.
633 Friedman, S.P., (2005). Soil properties influencing apparent electrical conductivity: a review,
634 , 46(1-3), 45-70. https://doi.org/10.1016/j.compag.2004.11.001.
635 Gardner, W.H. (1986). : Book Editor(s): Arnold Klute, Book Series:SSSA Book Series, chap.
636 21. https://doi.org/10.2136/sssabookser5.1.2ed.c21.
637 Gebbers, R., and Adamchuk, V.I. (2010). Precision Agriculture and Food Security. Science,
638 327, 828-831. https://doi.org/10.1126/science.1183899.
639 Ghanbarian, B., Hunt, A.G., Skaggs, T.H. and Jarvis, N. (2017). Upscaling soil saturated
640 hydraulic conductivity from pore throat characteristics. Advances in Water Resources,
641 104, 105-113. https://doi.org/10.1016/j.advwatres.2017.03.016.
642 Ghorbani, A., Camerlynck, C. and Florsch, N. (2009). CR1Dinv: A Matlab program to invert
643 1D spectral induced polarization data for the Cole–Cole model including electromagnetic
644 effects. Computer and Geosciences, 35(2), 255-266.
645 https://doi.org/10.1016/j.cageo.2008.06.001
646 Ghorbani, A., Revil, A., Coperey, A., Soueid Ahmed, A., Roque, S., Heap, M. J., Grandis, H.
647 and Viveiros, F. (2018). Complex conductivity of volcanic rocks and the geophysical
648 mapping of alteration in volcanoes. Journal of Volcanology and Geothermal Research,
649 357, 106–127. https://doi.org/10.1016/j.jvolgeores.2018.04.014.

650 Gouy, G. L. (1910). Sur la constitution de la charge électrique à la surface d'un électrolyte:
651 Journal de Physique Théorique et Appliquée, 9, 457–468.
652 https://doi.org/10.1051/jphystap:019100090045700.
653 Grote, K., Anger, C., Kelly, B., Hubbard, S. and Rubin, Y., (2010). Characterization of Soil
654 Water Content Variability and Soil Texture using GPR Groundwave Techniques. Journal
655 of Environmental and Engineering Geophysics, 15(3),
656 https://doi.org/10.2113/JEEG15.3.93.
657 Hazelton, PA. and Murphy, BW. (2007). Interpreting Soil Test Results: What do all the
658 numbers mean? CSIRO Publishing: Melbourne.
659 Huisman, J. A., Hubbard, S.S., Redman, J.D., and Annan, A.P. (2003). Measuring Soil Water
660 Content with Ground Penetrating Radar. Vadose Zone Journal, 2(4), 476-491.
661 Ikard, S., Revil, A., Schmutz, M., Karaoulis, M., Jardani, A., and Mooney, M. (2014).
662 Characterization of focused seepage through an earthfill dam using geoelectrical
663 methods: Groundwater, 52 (6), 952-965.
664 IPCC Special Report on Climate Change and Land (2019). An IPCC Special Report on
665 climate change, desertification, land degradation, sustainable land management, food
666 security,and greenhouse gas fluxes in terrestrial ecosystems. Eds: V. Masson-Delmotte,
667 P. Zhai, H.-O. Pörtner, D. Roberts, J. Skea, E. Calvo, B. P.R. Shukla, R. Slade, S.
668 Connors, R. van Diemen, M.Ferrat, E. Haughey, S. Luz, S. Neogi, M. Pathak, J. Petzold,
669 J. Portugal, P. Purvi, V. E. Huntley, K. Kissick, M. Belkacemi, J. Malley. 874 pp.
670 Jafarzadeh, A. A., Pal, M., Servati, M., FazeliFard, M. H., and Ghorbani, M. A. (2016).
671 Comparative analysis of support vector machine and artificial neural netw.ork models for
672 soil cation exchange capacity prediction: International Journal of Environmental Science
673 and Technology, 13, 87–96. https://doi.org/10.1007/s13762-015-0856-4.

674 Karaoulis, M., Revil, A., Tsourlos, P., Werkema, D.D., and Minsley, B.J. (2013). IP4DI: A
675 software for time-lapse 2D/3D DC-resistivity and induced polarization tomography.
676 Computers and Geosciences, 54, 164-170. https://doi.org/10.1016/j.cageo.2013.01.008.
677 Kemna, A., Binley, A., Cassiani, G., Niederleithinger, E., Revil, A., Slater, L., Williams,
678 K.H., Flores Orozco, A., Haegel, F.-H., Hördt, A., Kruschwitz, S., Leroux, V., Titov, K.
679 and Zimmermann, E. (2012). An overview of the spectral induced polarization method
680 for near-surface applications. Near Surface Geophysics, 10, 453-468.
681 https://doi.org/10.3997/1873-0604.2012027.
682 Kurniawan, B. (2005). Shaly sand interpretation using CEC-dependent petrophysical
683 parameters. PhD Thesis, Louisiana State University, 201 pp.
684 https://digitalcommons.lsu.edu/gradschool_dissertations/2384.
685 Lambe T. W., (1955). The Permeability of Fine-Grained Soils, in *Symposium on Permeability*
686 *of Soils*, ed. R. Subcommittee (West Conshohocken, PA: ASTM International), 56-
687 67. https://doi.org/10.1520/STP46165S.
688 Legchenko, A., Baltassat, J.-M., Beauce, A. and Bernard, J. (2002). Nuclear magnetic
689 resonance as a geophysical tool for hydrogeologists: Journal of Applied Geophysics,
690 50(1-2), 21-46. https://doi.org/10.1016/S0926-9851(02)00128-3.
691 Li, N., Zare, E., Huang, J., & Triantafilis, J. (2018). Mapping soil cation-exchange capacity
692 using Bayesian modeling and proximal sensors at the field scale. Soil Science Society of
693 America Journal, 82(5), 1203-1216. https://doi.org/10.2136/sssaj2017.10.0356.
694 Lorne, B., Perrier, F., and Avouac, J.-P. (1999). Streaming potential measurements. 1.
695 Properties of the electrical double layer from crushed rock samples. Journal of
696 Geophysical Research, 104(17), 857-877. https://doi.org/10.1029/1999JB900156.
697 Martinez, G., Huang, J., Vanderlinden, K., Giráldez, J. V., & Triantafilis, J. (2018). Potential
698 to predict depth-specific soil-water content beneath an olive tree using electromagnetic

699 conductivity imaging. Soil Use and Management, 34(2), 236-248.
700 https://doi.org/10.1111/sum.12411.
701 Mosegaard, K., and Tarantola, A. (1995). Monte Carlo sampling of solutions to inverse
702 problems. Journal of Geophysical Research, 100, no. B7, 12431–12447,
703 https://doi.org/10.1029/94JB03097.
704 Muzzamal M; Huang J; Nielson R; Sefton M; Triantafilis J. (2018). Mapping soil particle-size
705 fractions using additive log-ratio (ALR) and isometric log-ratio (ILR) transformations
706 and proximally sensed ancillary data. Clays and Clay Minerals, 66, 9-27,
707 http://dx.doi.org/10.1346/CCMN.2017.064074.
708 Oliver, D. P., Bramley, R. G. V., Riches, D., Porter, I., and Edwards, J. (2013). Review: soil
709 physical and chemical properties as indicators of soil quality in Australian viticulture.
710 Australian Journal of Grape and Wine Research, 19(2), 129-139.
711 https://doi.org/10.1111/ajgw.12016.
712 Olhoeft, G.R. (1981). Electrical Properties of Rocks. Physical properties of rocks and
713 minerals. 17p.
714 Parfitt, R.L., Giltrap, D.J., and Whitton, J.S. (1995). Contribution of organic-matter and clay-
715 minerals to the cation-exchange capacity of soils: Communications in Soil Science and
716 Plant Analysis, 26, 1343–1355.
717 Parfitt, R.L., Giltrap, D;J., and Whitton, J.S., (2008). Contribution of organic matter and clay
718 minerals to the cation exchange capacity of soils, Communications in Soil Science and
719 Plant Analysis, 26(9-10), 1343-1355. https://doi.org/10.1080/00103629509369376.
720 Pennington, V.E., Palmquist, K.A., Bradford, J.B., and Lauenroth, W.K. (2017). Climate and
721 soil texture influence patterns of forb species richness and composition in big sagebrush
722 plant communities across their spatial extent in the western U.S. Plant ecology, 218, 957–
723 970.

724 Petersen, H., Fleige, H., Rabbel, W. and Horn, R. (2005). Applicability of geophysical
725 prospecting methods for mapping of soil compaction and variability of soil texture on
726 farm land. Journal of Plant Nutrition and Soil Science-Zeitschrift Fur Pflanzenernahrung
727 Und Bodenkunde, 168 (1). pp. 68-79. https://doi.org/10.1002/jpin.2004.21282.
728 Platel, J.P., Esteve, A. and Tomera, L. (2004). Cartographie de l'aléa retrait-gonflement des
729 argiles dans le département de la Gironde. Rapport final. BRGM/RP-53382-FR, 236 pp.
730 Revil, A., Darot, M., Pezard, P.A., and Becker, K. (1996). Electrical conduction in oceanic
731 dikes, Hole 504B, Ed. by Alt, J.C., Kinoshita, H., *et al*., Proc. ODP Sci. Res., 148,
732 College Station, TX (ODP), 297-305.
733 Revil, A., Cathles, L.M., Losh, S., and Nunn, J.A. (1998). Electrical conductivity in shaly
734 sands with geophysical applications, Journal of Geophysical Research, 103(B10), 23,925-
735 23,936.
736 Revil, A., Hermitte, D., Spangenberg, E., and Cochémé, J. J. (2002). Electrical properties of
737 zeolitized volcaniclastic materials. Journal of Geophysical Research, 107(B8), 2168.
738 https://doi.org/10.1029/2001JB000599.
739 Revil, A., Karaoulis, M., Johnson, T., and Kemna, A. (2012). Review: Some low-frequency
740 electrical methods for subsurface characterization and monitoring in hydrogeology.
741 Hydrogeology Journal, **20(4)**, 617–658. https://doi.org/10.1007/s10040-011-0819-x.
742 Revil, A. (2013a). On charge accumulation in heterogeneous porous rocks under the influence
743 of an external electric field. Geophysics, 78(4), D271–291.
744 https://doi.org/10.1190/geo2012-0503.1.
745 Revil, A., (2013b). Effective conductivity and permittivity of unsaturated porous materials in
746 the frequency range 1mHz-1GHz. Water Resour. Res., 49, 306-327.
747 https://doi.org/10.1029/2012WR012700.

748 Revil., A. (2014). Comment on: "On the relationship between induced polarization and
749 surface conductivity: Implications for petrophysical interpretation of electrical
750 measurements" (A. Weller, L. Slater, and S. Nordsiek, Geophysics, 78, no. 5, D315–
751 D325), Geophysics, 79, no. 2, X1-X5, doi: 10.1190/GEO2013-0300.1.
752 Revil A., N. Florsch, and D. Mao (2015a). Induced polarization response of porous media
753 with metallic particles — Part 1: A theory for disseminated semiconductors. Geophysics,
754 80(5), D525–D538. https://doi.org/10.1190/GEO2014-0577.1.
755 Revil, A., Binley, A., Mejus, L., and Kessouri, P. (2015b). Predicting permeability from the
756 characteristic relaxation time and intrinsic formation factor of complex conductivity
757 spectra: Water Resour. Res., 51. https://doi.org/10.1002/2015WR017074.
758 Revil, A., Coperey, A., Shao, Z., Florsch, F., Fabricius, L. I., Deng, Y., and Delsman, J. R.
759 (2017a). Complex conductivity of soils. Water Resources Research, 53(8), 7121–47.
760 https://doi.org/10.1002/2017WR020655.
761 Revil A., Le Breton, M., Niu, Q., Wallin, E., Haskins, E., and Thomas, D.M. (2017b).
762 Induced polarization of volcanic rocks. 1. Surface versus quadrature conductivity.
763 Geophysical Journal International, 208, 826–844. https://doi.org/10.1093/gji/ggw444.
764 Revil, A., Le Breton, M., Niu, Q., Wallin, E., Haskins, E., and Thomas, D.M. (2017c).
765 Induced polarization of volcanic rocks. 2. Influence of pore size and permeability.
766 Geophysical Journal International, 208, 814–825. https://doi.org/10.1093/gji/ggw382.
767 Revil, A., Coperey A., Deng Y., Cerepi A., and Seleznev, N. (2018a), Complex conductivity
768 of tight sandstones, Geophysics, 83, 2, E55-E74.. https://doi.org/10.1190/GEO2017-
769 0096.1.
770 Revil A., Y. Qi, A. Ghorbani, A. Soueid Ahmed, T. Ricci, and P. Labazuy (2018b), Electrical
771 conductivity and induced polarization investigations at Krafla volcano, Iceland, Journal

of Volcanology and Geothermal Research, 368, 73–90. https://doi.org/10.1016/j.jvolgeores.2018.11.008.

Revil A., Qi Y., Ghorbani A., Gresse M., and Thomas D.M. (2021), Induced polarization of volcanic rocks. 5. Imaging the temperature field of shield volcanoes: Geophys. J. Int., 225, 1492–1509, https://doi.org/10.1093/gji/ggab039.

Robinet, J., von Hebel, C., Govers, G., van der Kruk, J., Minella, J. P. G., Schlesner, A., Ameijeiras-Marino, Y., and Vanderborght, J. (2018). Spatial variability of soil water content and soil electrical conductivity across scales derived from Electromagnetic Induction and Time Domain Reflectometry: Geoderma, 314, 160-174.

Rubin, M. and Hubbard, S.S. (2005). Hydrogeophysics. Water Science and Technology Library, 50, 518 pp.

Sainju, U. M., and Singh, P. (1997). Winter cover crops for sustainable agricultural systems: influence on soil properties, water quality, and crop yields. Hort Science, 32(1), 21-28.

Sen, P. N., Straley, C., Kenyon, W. E., and Whittingham, M. S. (1990). Surface-to-volume ratio, charge density, nuclear magnetic relaxation, and permeability in clay-bearing sandstones. Geophysics, 55(1), 61-69.

Schmutz, M., Ghorbani, A., Vaudelet, P., and Blondel, A. (2014). Cable arrangement to reduce electromagnetic coupling effects in spectral-induced polarization studies. Geophysics, **79**(2). https://doi.org/10.1190/geo2013-0301.1.

Shah P. and D. Singh (2005). Generalized Archie's law for estimation of soil electrical conductivity, Journal of ASTM International 2(5), 1-20. https://doi.org/10.1520/JAI13087.

Soueid Ahmed, A., Revil, A., Abdulsamad, F., Steck, B., Vergniault, C., and Guihard, V. (2020). Induced polarization as a tool to non-intrusively characterize embankment

796 hydraulic properties. Engineering Geology, 271, 105604,
797 https://doi.org/10.1016/j.enggeo.2020.105604.
798 Stern, O. (1924). Zur Theorie der elektrolytischen doppelschicht, 30, 21-22, 508-516,
799 https://doi.org/10.1002/bbpc.192400182.
800 Titov, K., Komarov, V., Tarasov, V., Levitski, A. (2002). Theoretical and experimental study
801 of time domain-induced polarization in water-saturated sands, J. Appl. Geophys. ,50 (4),
802 417–433. http://dx.doi.org/10.1016/S0926-9851(02)00168-4.
803 Topp, G.C. (2003). State of the art of measuring soil water content. Hydrol. Process. 17,
804 2993–2996.
805 Tregoat, O. (2007). Cartographie des sols du vignoble de Château la Louviere. Carte
806 pédologique et notice, 52 pp.
807 Van Voorhis, G. D., Nelson P. H., and Drake T. L. (1973). Complex resistivity spectra of
808 porphyry copper mineralization. Geophysics, 38(1), 49–60.
809 https://doi.org/10.1190/1.1440333.
810 Van Leeuwen, C. (2010). Soils and terroir expression in wines. In: Landa E., Feller C. (eds)
811 Soil and Culture. Springer, Dordrecht, 453-465. https://doi.org/10.1007/978-90-481-
812 2960-7_28.
813 Vaudelet P., A. Revil, M. Schmutz, M. Franceschi, and P. Bégassat (2011a). Induced
814 polarization signature of the presence of copper in saturated sands, Water Resources
815 Research, 47, W02526, doi:10.1029/2010WR009310.
816 Vaudelet P., Revil, A., M. Schmutz, M. Franceschi, and P. Bégassat, 2011b. Changes in
817 induced polarization associated with the sorption of sodium, lead, and zinc on silica
818 sands, Journal of Colloid and Interface Science, 360, 739-752.
819 Vinegar, H., and Waxman, M. (1984). Induced polarization of shaly sands. Geophysics, 49(8),
820 1267–87. https://doi.org/10.1190/1.1441755.

821 Weller, A., Slater, L., and Nordsiek, S. (2013). On the relationship between induced
822 polarization and surface conductivity: Implications for petrophysical interpretation of
823 electrical measurements. Geophysics, 78(5), D315–D325.
824 https://doi.org/10.1190/geo2013-0076.1.
825 Yolcubal, I., Brusseau, M.L., Artiola, J.F., Wierengal, P., and Wilson, G. (2004).
826 Environmental physical properties and processes. Environmental monitoring and
827 characterization, 207-239.
828 Zare, E., Arshad, M., Zhao, D., Nachimuthu, G., & Triantafilis, J. (2020). Two-dimensional
829 time-lapse imaging of soil wetting and drying cycle using EM38 data across a flood
830 irrigation cotton field. Agricultural Water Management, 241.
831 https://doi.org/10.1016/j.agwat.2020.106383
832 Zhao, D., Li, N., Zare, E., Wang, J., & Triantafilis, J. (2020a). Mapping cation exchange
833 capacity using a quasi-3d joint inversion of EM38 and EM31 data. Soil and Tillage
834 Research, 200. https://doi.org/10.1016/j.still.2020.104618.
835 Zhao, X., Arshad, M., Li, N., Zare, E., & Triantafilis, J. (2020b). Determination of the
836 optimal mathematical model, sample size, digital data and transect spacing to map CEC
837 (Cation exchange capacity) in a sugarcane field. Computers and Electronics in
838 Agriculture, 173. https://doi.org/10.1016/j.compag.2020.105436.
839 Zhao, Y., Zimmermann, E., Huisman, J. A., Treichel, A., Wolters, B., van Waasen, S., and
840 Kemna, A. (2013). Broadband EIT borehole measurements with high phase accuracy
841 using numerical corrections of electromagnetic coupling effects. Measurement Science
842 and Technology, 24(8), 085005.
843 Zimmermann, E., Kemna, A., Berwix, J., Glaas, W., Münch, H. M., and Huisman, J. A.
844 (2008). A high-accuracy impedance spectrometer for measuring sediments with low

845 polarizability. Measurement Science and Technology, 19(10), 105603.
846 https://doi.org/10.1088/0957-0233/19/10/105603.
847

Appendix A. Inversion of the Cole Cole parameters

We consider that the grain size distribution is bimodal with coarse grains (sands) and small grains (clays). The corresponding double Cole-Cole equation is written as

$$\sigma^* = \sigma_\infty \left(1 - \frac{M_1}{1 + (i\omega\tau_1)^{c_1}} - \frac{M_2}{1 + (i\omega\tau_2)^{c_2}} \right) \quad \text{(A1)}$$

where M_1 and M_2 denote the chargeabilities, c_1 and c_2 are the two Cole-Cole exponents (dimensionless), and τ_1 and τ_2 are the (relaxation) time constants (in s). The index 1 and 2 refer to lower (sand) and higher (clay) frequency dispersions, respectively. The (integrated or total) normalized chargeability M_n is obtained as $M_n = \sigma_\infty \left(M_1 + M_2 \right)$.

The complex conductivity spectra can be inverted using equation (A1) and the non-linear iterative approach of Mosegaard and Tarantola (1995) based on a Monte Carlo Markov Chain (MCMC) sampling algorithm. The Bayesian approach describes the prior information we have on the model vector, using a probability density P(**m**) where **m** denotes the model vector of unknown parameters **m** = [log(σ_0); M_1; c_1; log(τ_1); M_2; c_2; log(τ_2)]. Then, the algorithm combines this information with the observed data vector $\mathbf{d}_{obs}$ and with the information provided by the double Cole-Cole model, L(**m**), as described by equation (A1). In Bayesian theory, the posterior probability density σ(**m**) equals the prior probability density $P(\mathbf{m})$ times a likelihood function $L(\mathbf{m})$, which measures the fit between observed data and data predicted from the model vector **m**, i.e, $\sigma(\mathbf{m}) = hP(\mathbf{m})L(\mathbf{m})$, where h denotes a normalization constant. We describe the complex conductivity data by a vector of observed values $\mathbf{d}_{obs}$ characterized by Gaussian uncertainties associated with the measurement procedure. We consider the case of independent, identically distributed Gaussian uncertainties. Then the likelihood function describing the experimental uncertainties is given by:

871 $$L(\mathbf{m}) = k \exp\left(-\frac{S(\mathbf{m})}{s^2} \right), \quad \text{(A2)}$$

872 where s^2 is the total noise variance and where the misfit function is given by

873 $$S(\mathbf{m}) = \frac{1}{2} \sum_{i=1}^{n} \left(g^i(\mathbf{m}) - d^i_{obs} \right)^2, \quad \text{(A3)}$$

874 where **d** is data vector, g(**m**)=σ^* is the forward modeling function, and s^2 is the same for all
875 data values. The acceptance probability for a perturbed model becomes

876 $$P_{accept} = \begin{cases} 1 \text{ if } S(\mathbf{m}_{new}) \le S(\mathbf{m}_{old}) \\ \exp\left(-\frac{\Delta S}{s^2} \right) \text{if } S(\mathbf{m}_{new}) > S(\mathbf{m}_{old}) \end{cases} \quad \text{(A4)}$$

877 where $\Delta S = S(\mathbf{m}_{new}) - S(\mathbf{m}_{old})$. The observed data used in the inversion process were the real
878 and imaginary parts of the complex conductivity calculated from the amplitude and phase
879 values measured at different frequencies.

880 We assume that the standard deviation, *s*, is equal to 10% of the measured complex
881 conductivity values (i.e., corresponding to the maximum of the experimental error). Locally
882 uniform law (the probability distribution is constant over an interval [θ_1, θ_2] and vanishes
883 elsewhere) is used to describe the prior probability density on the model parameters. Interval
884 ranges for Cole-Cole model parameters are: σ_0 = [10^{-4}; 100] S m^{-1}, M_1 and M_2, c_1 and c_2 have
885 the same interval [0 1], τ_1=[10^{-5}, 10^5] s, and τ_2=[10^{-15}, 10^{-4}] s. At the end of the inversion
886 algorithm, we compute the Root Mean Square (RMS) error:

887 $$\mathrm{RMS}^2 = \frac{1}{n} \sum_{i=1}^{n} \left(\frac{g^i(\mathbf{m}) - d^i_{obs}}{d^i_{obs}} \right)^2, \quad \text{(A5)}$$

888 where *n* denotes the number of measurements. The results are reported in Table 2.
889

Tables

Table 1. Physiochemical properties of the core samples. The quadrature conductivity σ" is reported at 32 Hertz (samples E1 to E19, pore water conductivity of 0.072 S m^{-1} at 25°C, NaCl, sample REM pore water conductivity of 0.12 S m^{-1} at 25°C, NaCl). There is no sample labeled E16. The quantity ϕ denotes the porosity, CEC denotes the Cation Exchange Capacity, F denotes the formation factor, σ_S denotes the surface conductivity, M_n(1 Hz, 1 kHz) is the (partial) normalized chargeability determined at the lowest salinity and between 1 Hertz and 1 kHz. The main grain size corresponds to the peak of the distribution.

Core ID	ϕ (-)	CEC (meq/100g)	F (-)	σ_S (S/m)	M_n(1 Hz, 1 kHz) (S/m)	σ" (S/m)	Main grain size (μm)
E1	0.35	11.9	4.97	0.042	0.0049	0.0010	105
E2	0.36	9.53	5.80	0.032	0.0026	0.0006	98
E3	0.36	7.21	3.97	0.0107	0.0010	0.0003	63
E4	0.39	16.1	6.66	0.0771	0.0054	0.0013	88
E5	0.44	16.6	5.71	0.0932	0.0036	0.0008	40
E6	0.41	15.5	5.90	0.092	0.0055	0.0012	40
E7	0.39	7.82	3.84	0.0565	0.0034	0.0007	4
E8	0.43	7.24	3.54	0.0333	0.0021	0.0005	8
E9	0.42	11.5	3.16	0.0352	0.0025	0.0002	101
E10	0.43	7.67	5.40	0.0603	0.0027	0.0006	8
E11	0.40	7.3	4.18	0.0384	0.0021	0.0005	100
E12	0.51	20	4.89	0.114	0.0090	0.0021	40
E13	0.52	19.9	2.77	0.0503	0.0036	0.0014	125
E14	0.44	15.8	4.73	0.085	0.0054	0.0012	125
E15	0.43	9.77	6.65	0.155	0.0062	0.0019	125
E17	0.48	17.9	3.97	0.260	0.0147	0.0041	75
E18	0.45	12.3	7.24	0.186	0.0073	0.0017	93
E19	0.44	11.5	2.94	0.0031	0.0003	0.0004	125
REM	0.26	2.6	9.10	0.031	0.00024	0.00085	-

900 **Table 2.** Double Cole Cole parameters obtained for the core samples at the lowest salinity.

Core ID	σ_∞ (S/m)	M_1 (-)	M_2 (-)	c_1 (-)	c_2 (-)	τ_1 (s)	τ_2 (s)	RMS (%)	Texture GPA [(1)]
E1	0.060	0.094	0.034	0.442	0.482	0.032	5.7e-05	0.19	SS
E2	0.045	0.062	0.069	0.409	0.466	0.020	2.3e-05	0.11	SS
E3	0.032	0.066	0.098	0.357	0.492	0.011	2.3e-06	0.24	Sl
E4	0.082	0.085	0.049	0.407	0.473	0.021	4.6e-05	0.16	SS
E5	0.099	0.041	0.091	0.320	0.470	0.008	7.4e-06	0.16	Ls
E6	0.107	0.068	0.075	0.351	0.514	0.015	1.4e-05	0.14	Ls
E7	0.082	0.034	0.089	0.371	0.395	0.063	1.3e-05	0.23	LL
E8	0.059	0.019	0.069	0.465	0.469	0.113	8.9e-05	0.25	Ls
E9	0.020	0.053	0.072	0.462	0.481	0.035	2.2e-06	0.74	SS
E10	0.075	0.043	0.111	0.369	0.420	0.019	20e-06	0.35	Sl
E11	0.059	0.029	0.091	0.446	0.463	0.072	1.1e-05	0.46	Sl
E12	0.120	0.089	0.061	0.446	0.642	0.005	3.9e-05	0.34	Ls
E13	0.080	0.082	0.067	0.488	0.473	0.036	3.5e-05	0.39	Sl
E14	0.096	0.061	0.055	0.498	0.530	0.084	7.9e-05	0.61	Sl
E15	0.175	0.057	0.047	0.394	0.476	0.038	4.9e-05	0.14	Sl
E17	0.344	0.049	0.079	0.494	0.461	0.072	2.89e-05	0.62	Sl
E18	0.204	0.042	0.045	0.397	0.531	0.146	7.8e-05	0.34	Sl
E19	0.031	0.060	0.117	0.456	0.515	0.116	8.4e-06	0.61	Sl

901

902 [(1)] GEPPA is a French soil texture classification. The texture labels correspond to SS: pure sand, Sl:
903 silty sand, Ls: sandy silt, LL: pure silt.

904

905 **Table 3.** Comparison between the CEC determined in the laboratory for the core samples and the CEC
906 determined from the inverted field data using the petrophysical transforms described in the main text.
907 We need to remember that the comparison is only qualitative for various reasons (i) the spatial support
908 between the core sample (cm scale) and the field data (m scale) is not the same and (ii) the CEC of the
909 laboratory data include the CEC of humic substances (which does not impact the SIP data). For the
910 clay core sample, the CEC is taken from Table 4 (direct measurement with the cobalt hexamine
911 method) while the field CEC is the average of the CEC of the tomogram for the clay formation from
912 the geophysical field data.

913

Sample	Measured CEC (meq/100g)	Field CEC (meq/100g)	Texture GEPPA
E1	11.9	7.6	SS
E2	9.5	7.7	SS
E3	7.2	13.7	Sl
E4	16.1	10.7	SS
E5	16.6	10.5	Ls
E6	15.5	12.2	Ls
E7	7.8	13.0	LL
E8	7.2	13.1	Ls
E9	11.5	6.2	SS
E10, E11	7.7	8.2	Sl
E12	20	15	Ls
E13	15.8	12.1	Sl
E14	19.9	12.1	Sl
E15	9.8	15.6	Sl
E17	17.9	10.2	Sl
E18	12.3	12.6	Sl
E19	11.5	13.5	Sl
Clay	40.2	43±12	AA

914

915 **Table 4.** Physical properties of a clay core sample drilled in the vicinity of the test site in the
916 same clay formation.

Property	Clay end-member
CEC (meq/100g)	40.2
Soil type (GEPPA)	AA
Depth of extraction (m)	2.1-2.2
Clay (vol.%)	67.1
Silt (vol.%)	6.6
Sand (vol.%)	26.3

917
918

Figures

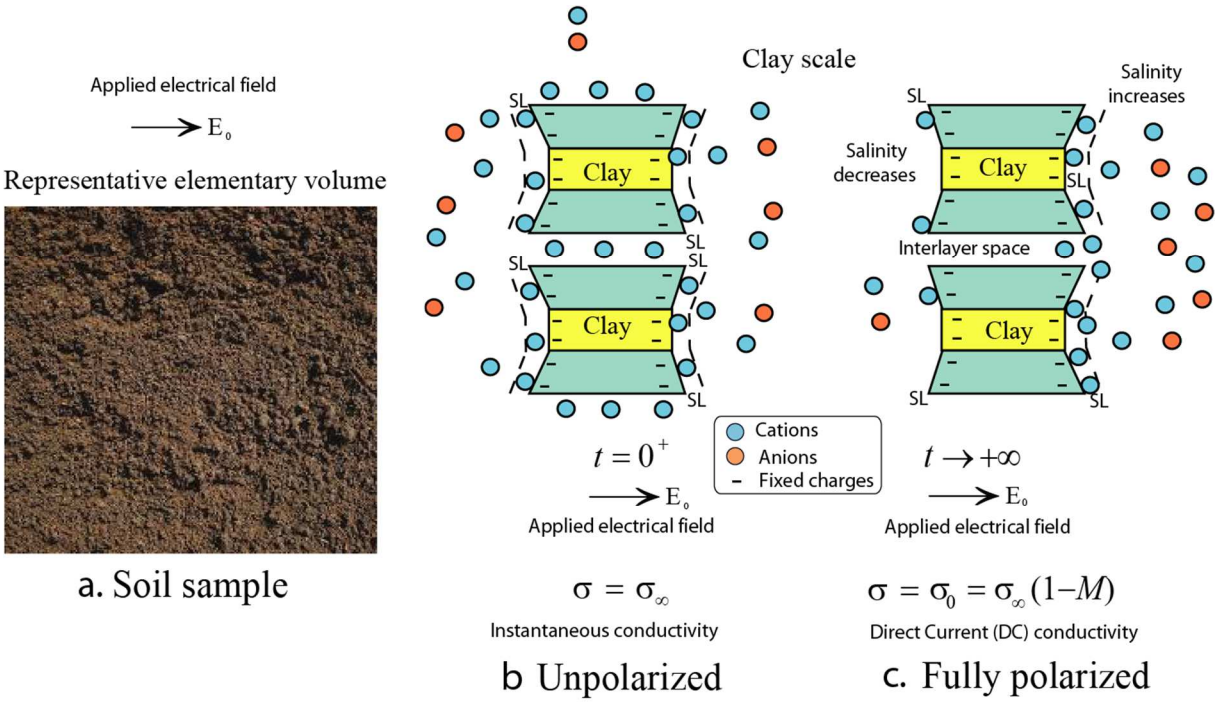

Figure 1. Polarization of the clay particles due to an applied (external) electrical field $\mathbf{E}_0$. **a.** Soil sample submitted to an applied electrical field $\mathbf{E}_0$. **b.** At the particle scale, the grains are surrounded by an electrical double layer (e.g., Gouy, 1910; Stern 1924). When the external electrical field is applied, the charge carriers are all mobile. They all participate to the surface (interfacial) conduction process (at t=0+ just after the shut down of the primary current). The instantaneous conductivity σ_∞ corresponds to this state. **c.** When the external electrical field has been applied for a long time, the clay particle gets fully polarized. The ionic charge carriers associated with the polarization of the clay do not contribute to the conduction process anymore. In this situation, the conductivity of the material corresponds to the Direct Current (DC) conductivity σ_0, which is necessarily smaller than the instantaneous conductivity. SL stands for the Stern Layer. M (dimensionless) denotes the chargeability.

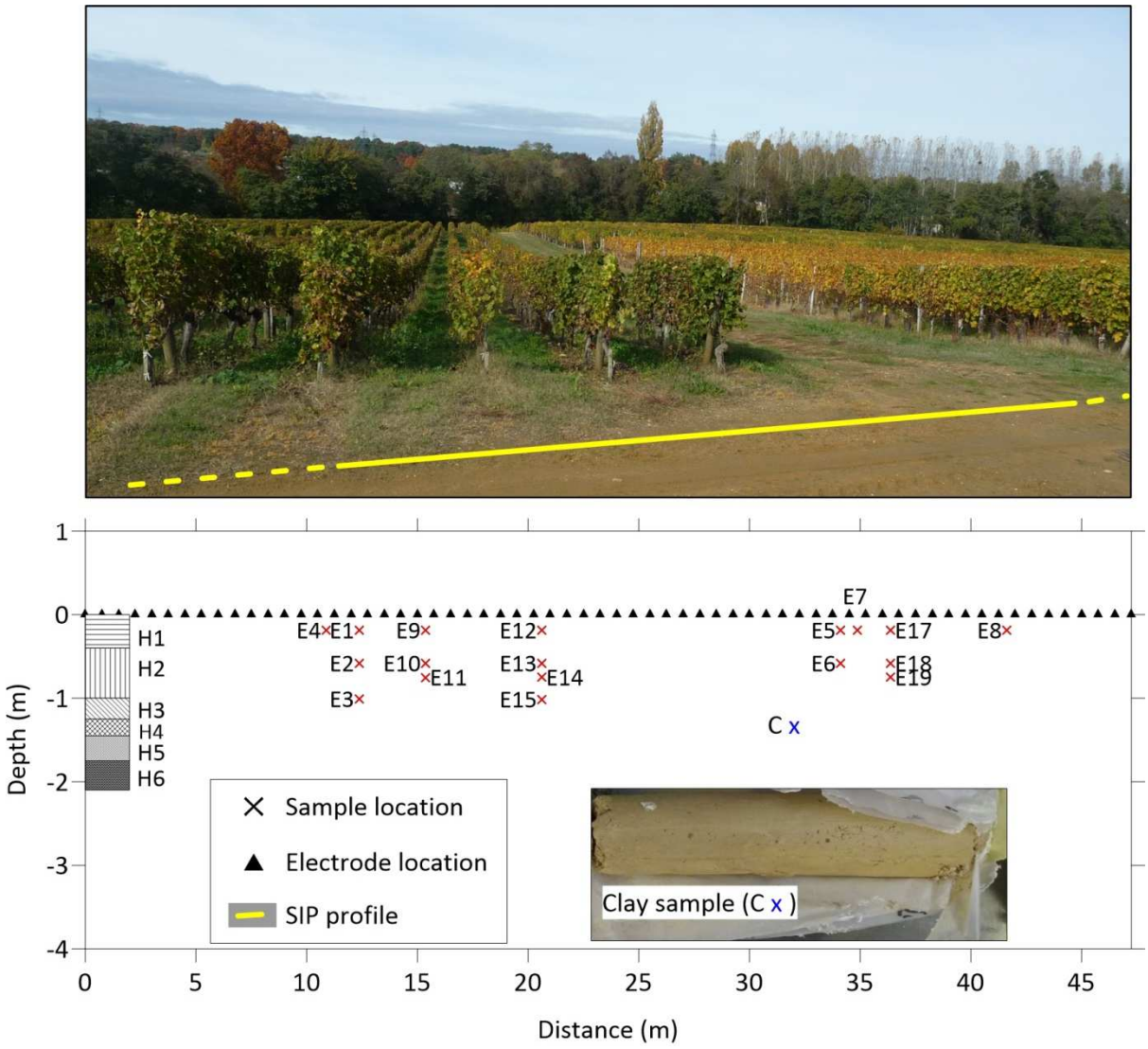

Figure 2. Description of the test site. Upper panel: Image showing the position of the geophysical profile in the vineyard. Lower panel: Six soil horizons (H1-H6) have been defined at the site. Soil samples (labeled E1 to E19) used for the petrophysical interpretation were extracted along the profile from Horizons H1 and H2. SIP stands for Spectral Induced Polarization.

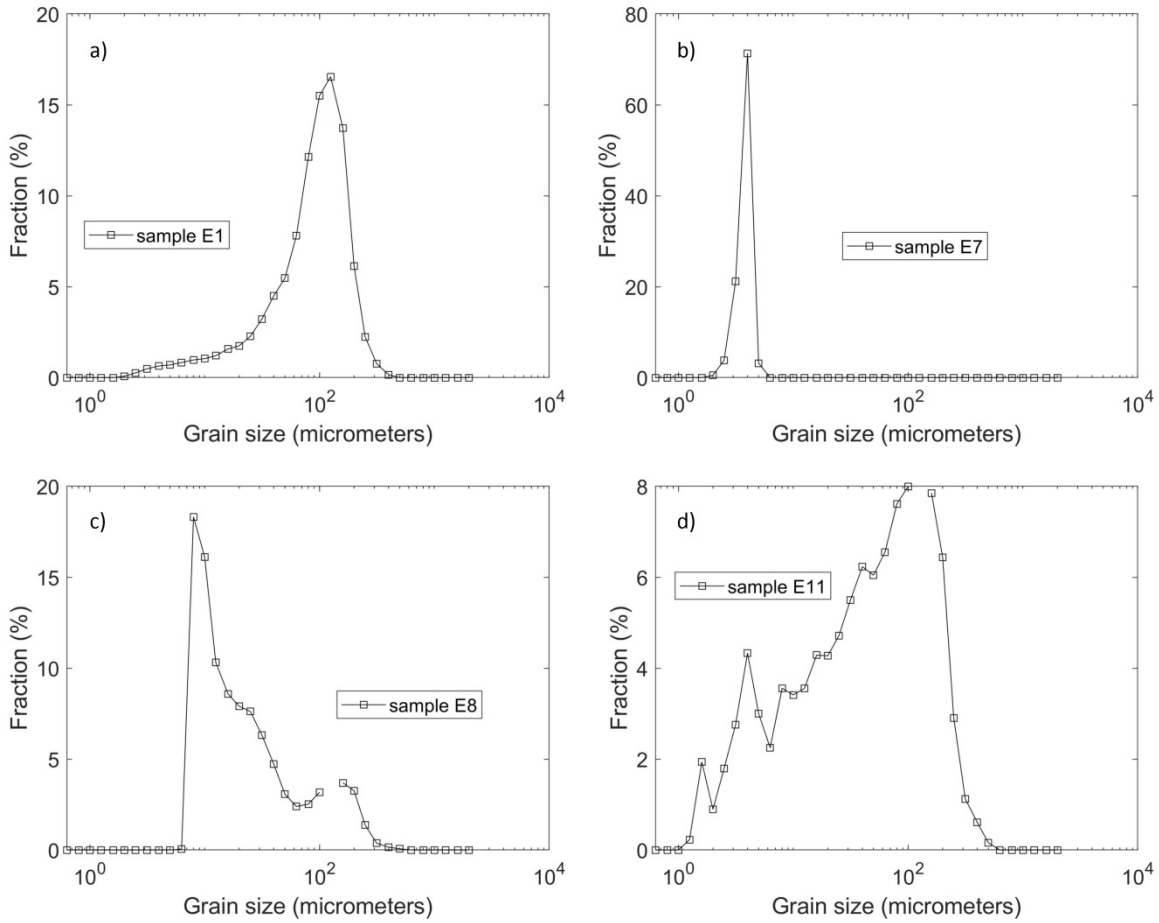

Figure 3. Grain size distribution of some selected core samples. **a.** Sample E1. **b.** Sample E7. **c.** Sample E8. **d.** Sample E11. The broadness of the grain size distribution can be very different between the different samples. The c-exponent of sample E7 is 0.39 consistent with the narrow grain size distribution exhibited by this core sample. The c_1-exponent of sample E11 is 0.30 consistent with a broad grain size distribution.

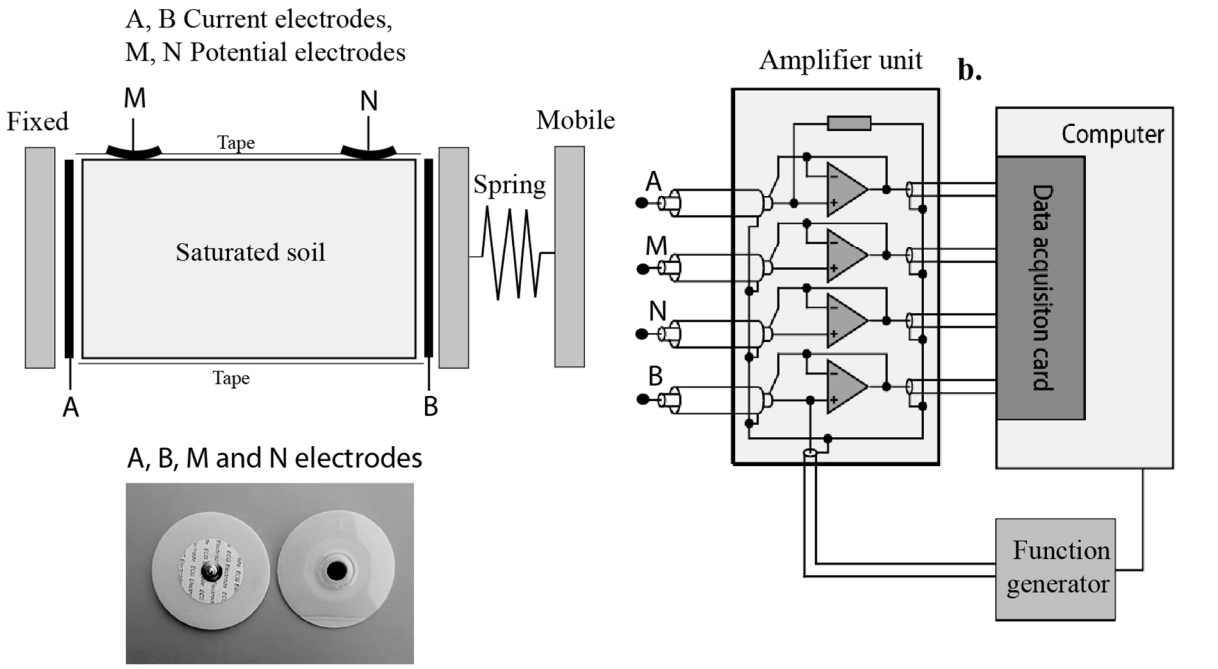

953 **a.** Complex conductivity cell **b.** ZEL-SIP04-V02 impedance meter
954

955

956 **Figure 4.** Spectral induced polarization measurements of a soil. **a.** Conductivity cell with the
957 electrodes. **b.** ZEL-SIP04-V02 impedance meter operating in the frequency range 1 mHz-45
958 kHz (Zimmerman et al., 2008). The precision in phase measurement of this instrument is ~0.1
959 mrad below 1 kHz. A test of the sample holder can be found in Revil et al. (2018a).
960
961

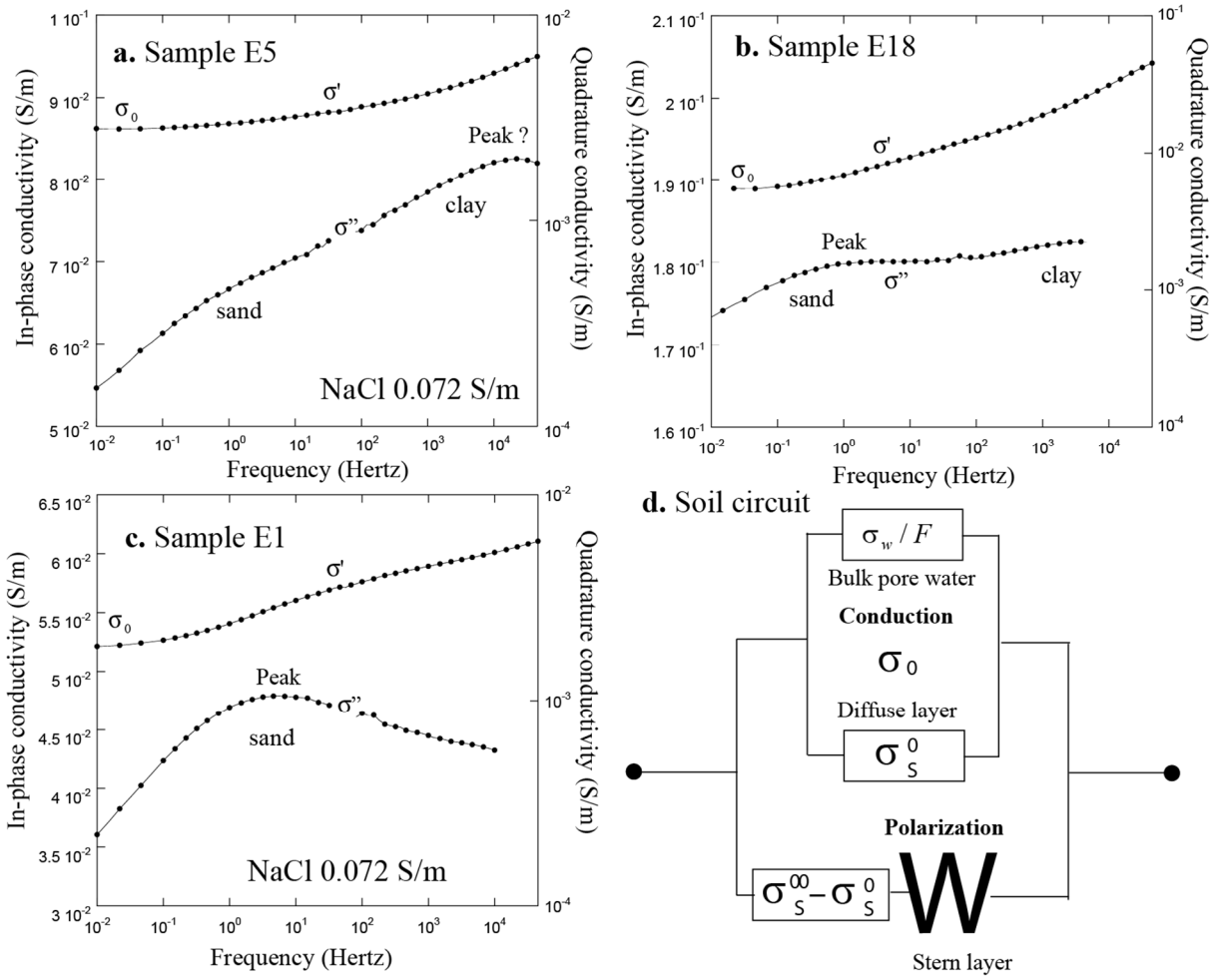

962

963

964 **Figure 5.** In-phase (σ') and quadrature conductivity (σ'') spectra of a soil. **a.** Sample E5. **b.**
965 Sample E18. **c.** Sample E1. **d.** Equivalent electrical circuit for a soil corresponding to equation
966 (4), where W denotes a Warburg-type capacitance corresponding to the polarization of the
967 Stern layer (the inner component of the electrical double layer). The conduction process
968 through a soil sample comprises two contributions: A bulk conductivity in the liquid pore
969 water and a surface conductivity associated with the electrical double layer. The quantities σ_S^{∞}
970 and σ_S^{0} represent the instantaneous and DC surface conductivity, respectively. The relaxation
971 time is associated with the polarization length scales (pore sizes or grain sizes) of the soil. The
972 data with a standard deviation higher than 5% have been removed.
973

974

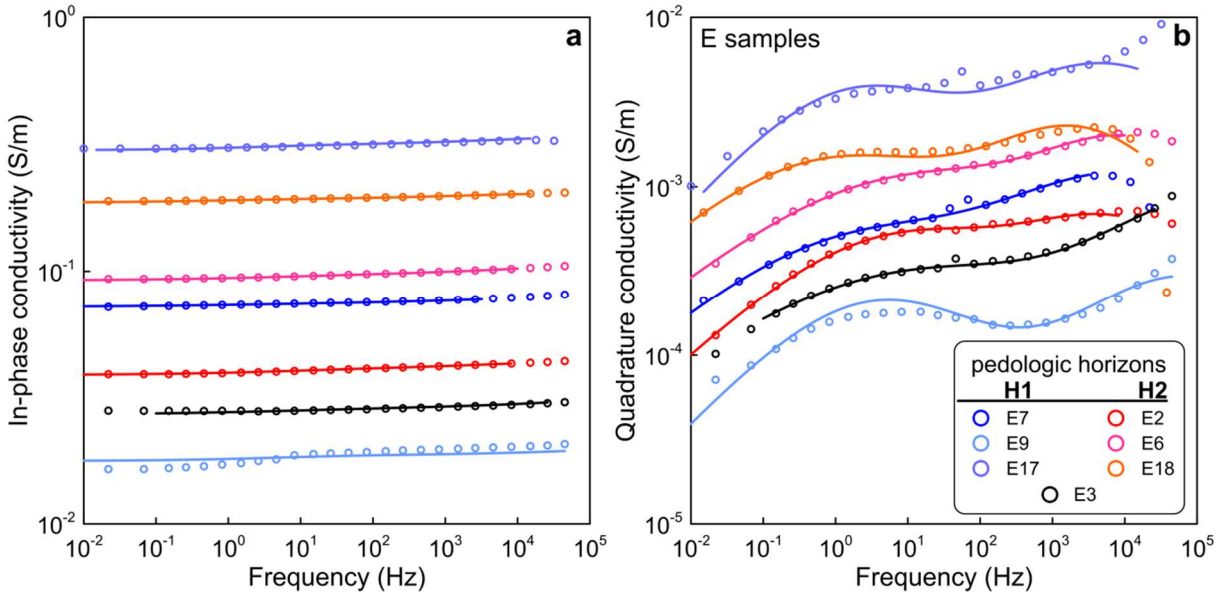

975

976

977 **Figure 6.** Selected examples of 7 complex conductivity spectra (in-phase and quadrature
978 conductivity) fitted with the double Cole Cole model described in Appendix A (plain lines, 6
979 core samples shown here). **a.** In-phase conductivity spectra. **b.** Quadrature conductivity
980 spectra. We have not used the high and low-frequency data with an RMS error >10%./ High
981 frequency errors are generally due to electromagnetic coupling effects while low frequency
982 errors are generally due to stability issues with the electrodes.

983

984

985

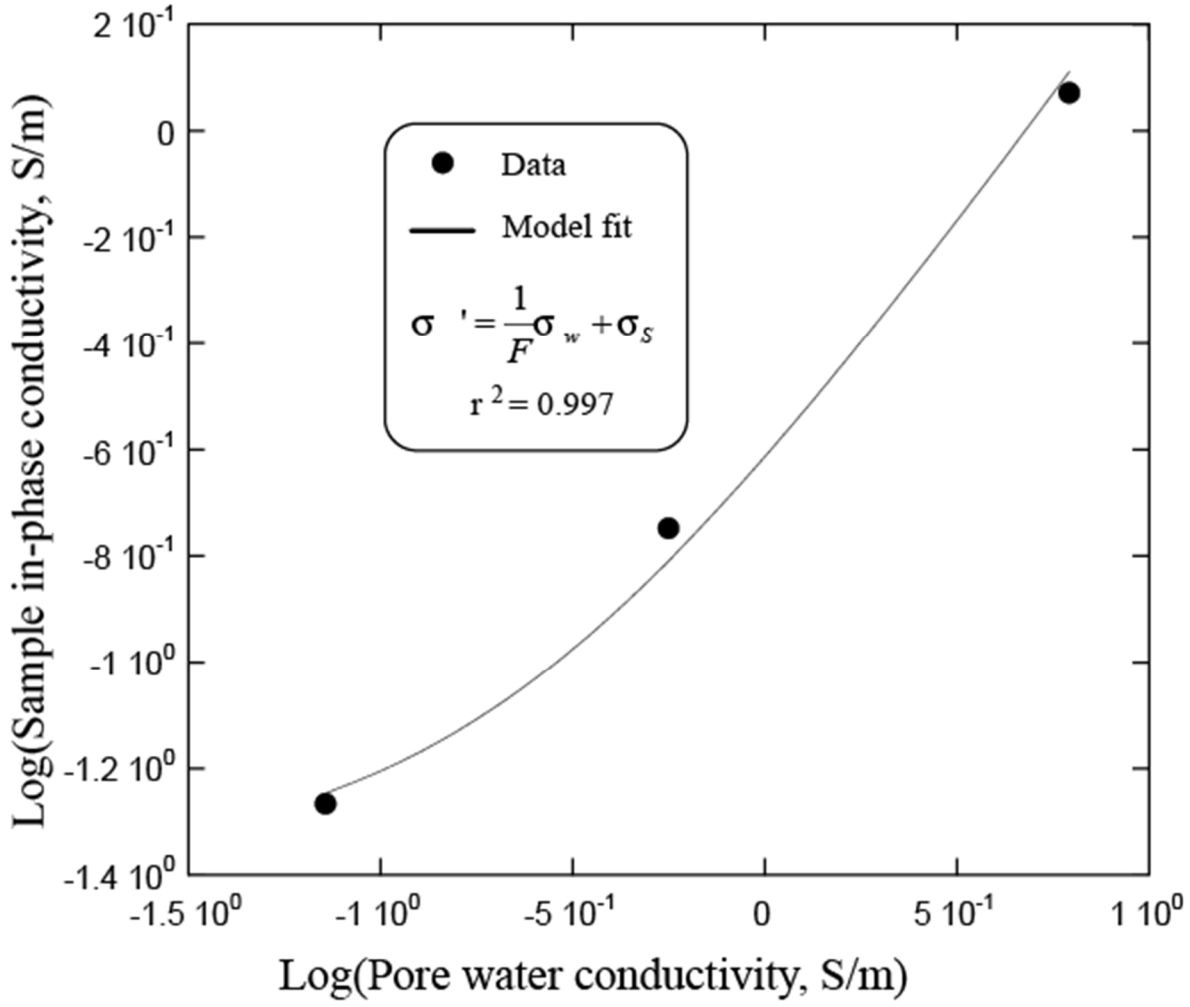

Figure 7. Determination of the formation factor F and surface conductivity σ_S using the in-phase conductivity of the core sample σ' (at 1 Hertz) versus the pore water conductivity σ_w. The fit of the conductivity model is done in a log-log plot to ensure the surface conductivity is correctly estimated. The formation factor and the surface conductivity are estimated for each sample (the formation factor as the slope of the trend). The fit is done by a non-linear least square regression technique in a log log space (see Revil et al., 2017a). The formation factor and surface conductivity values are reported in Table 1. Note that surface conductivity depends on the frequency but this dependence is small (less than 10%) owing the value of the chargeability M_1.

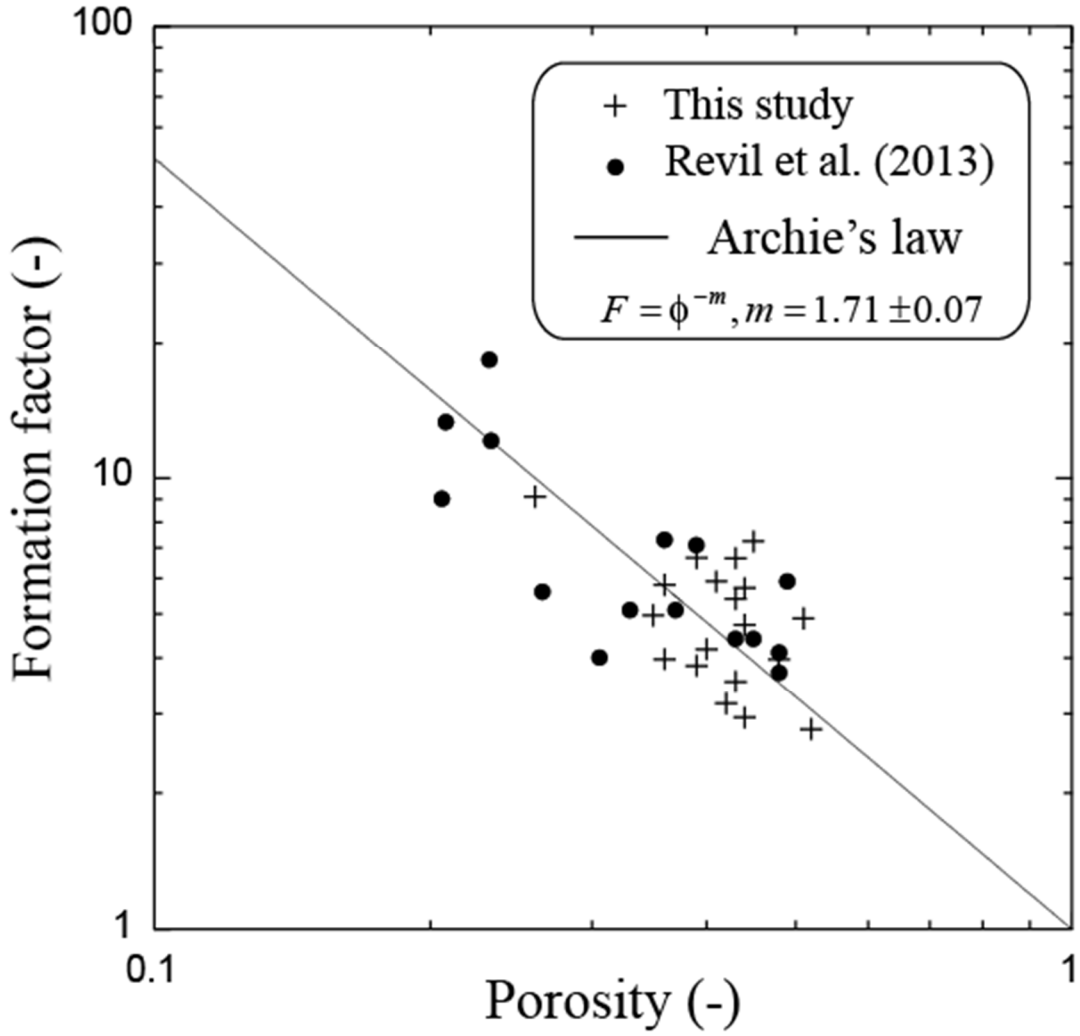

Figure 8. Fit of Archie's law between the formation factor F and the (connected) porosity ϕ for this study and the Revil et al. (2013) study on saprolitic soils to increase the data base on the low-porosity side. The best power-law regression (r^2 = 0.87) is used to obtain an average value of the cementation (porosity) exponent m using all the core samples. Using only the laboratory data from Table 1, we obtain m = 1.78 ± 0.35 (r^2 = 0.58)*:*

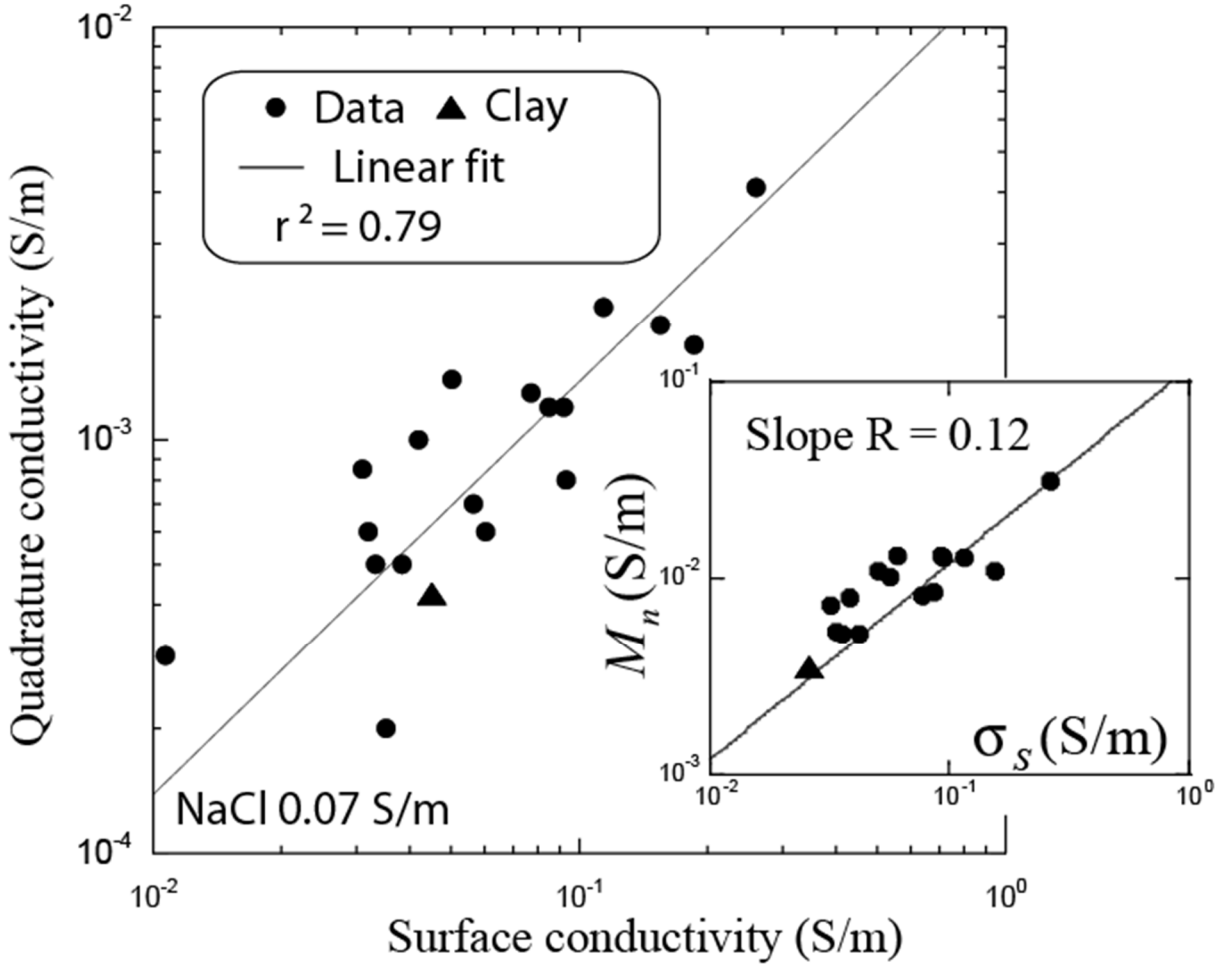

1013

1014 **Figure 9.** Quadrature versus surface conductivity (1 Hertz). For the soil samples we obtain –
1015 σ''/σ_S = 0.0140±0.001. Using $R = -\alpha\sigma''/\sigma_S$ and α = 8.8 (from equation 11, 6 orders of
1016 magnitude), we obtain R = 0.12. According to the dynamic Stern layer model, this trend is
1017 independent of the value of the formation factor and the porosity of the core samples. This
1018 confirms the results of Weller et al. (2013). Insert: Normalized chargeability M_n versus
1019 surface conductivity σ_S. The normalized chargeability is given from Table 2 as M_n =
1020 $(M_1+M_2)/\sigma_\infty$. The slope yields the following value for the dimensionless factor R = 0.12.
1021 The filled triangle corresponds to the clay pole investigated only through the field
1022 measurements assuming that the conductivity of the core sample is dominated by its surface
1023 conductivity component.
1024

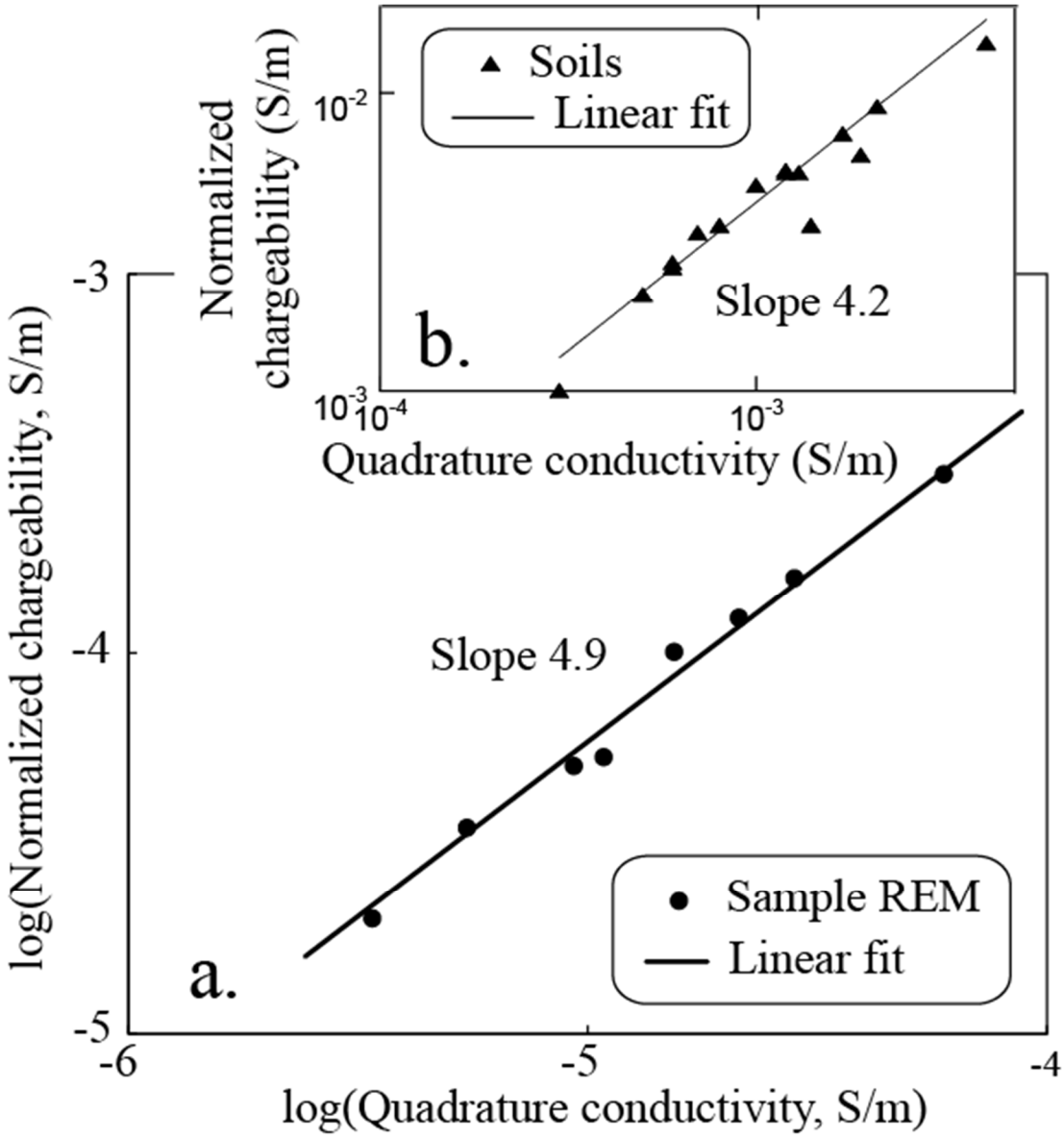

Figure 10. Relationship between the normalized chargeability (between the frequencies 1 Hertz and 1 kHz) and the quadrature conductivity at the geometric frequency of 32 Hertz. Different water saturations. **a.** REM Samples at different saturations. **b.** Soil samples at full water saturation. The slope α is found to be 4.9 for the REM samples (soil samples used as Ram Earth Material, REM, regression coefficient $r^2 = 0.97$) and 4.2 for the soils while the theory (equations 8 and 9, $r^2 = 0.92$) predicts a slope of 4.4. If the normalized chargeability would be determined over 6 orders of magnitude, we would expect to have $\alpha = 8.8$.

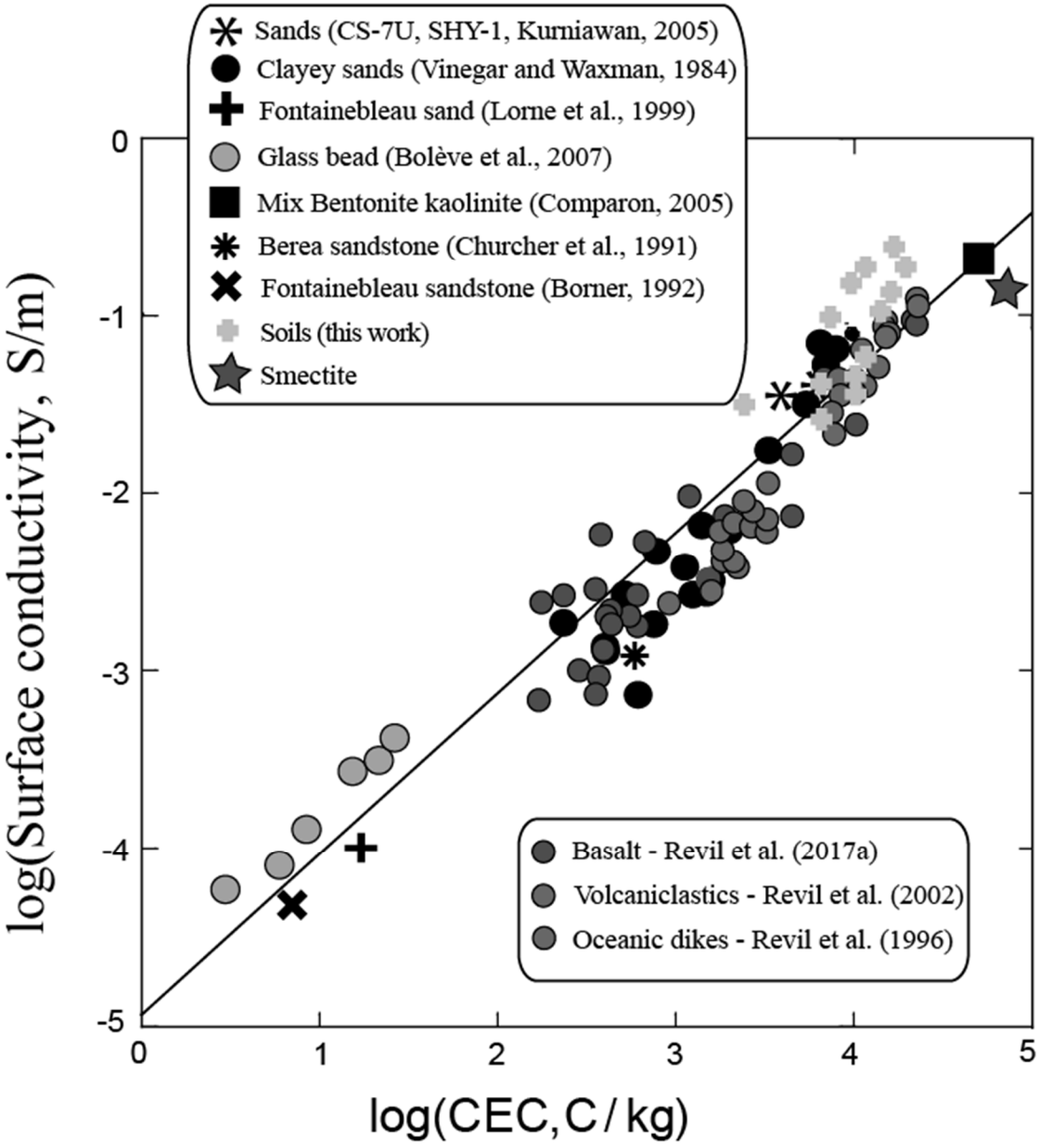

Figure 11. Surface conductivity versus cation exchange capacity (CEC) for high porosity (>0.20, saturated) core samples. The data from the literature are from Bolève et al. (2007, glass beads, NaCl), Vinegar and Waxman (1984, shaly sands, NaCl), Churcher et al. (1991) (CEC for the Berea sandstone), Lorne et al. (1999, Fontainebleau sand KCl), Kurniawan (2005, clean sand, Sample CS-7U), Börner (1992, sample F3 Fontainebleau sandstone), and Comparon (2005, mixtures of MX80 bentonite and kaolinite). The volcanic rock data are from Revil et al. (1996) and Revil et al. (2002). The overall trend confirms the linear dependence (r^2 = 0.94 in a log–log space) between the surface conductivity and the CEC for high porosity core samples.

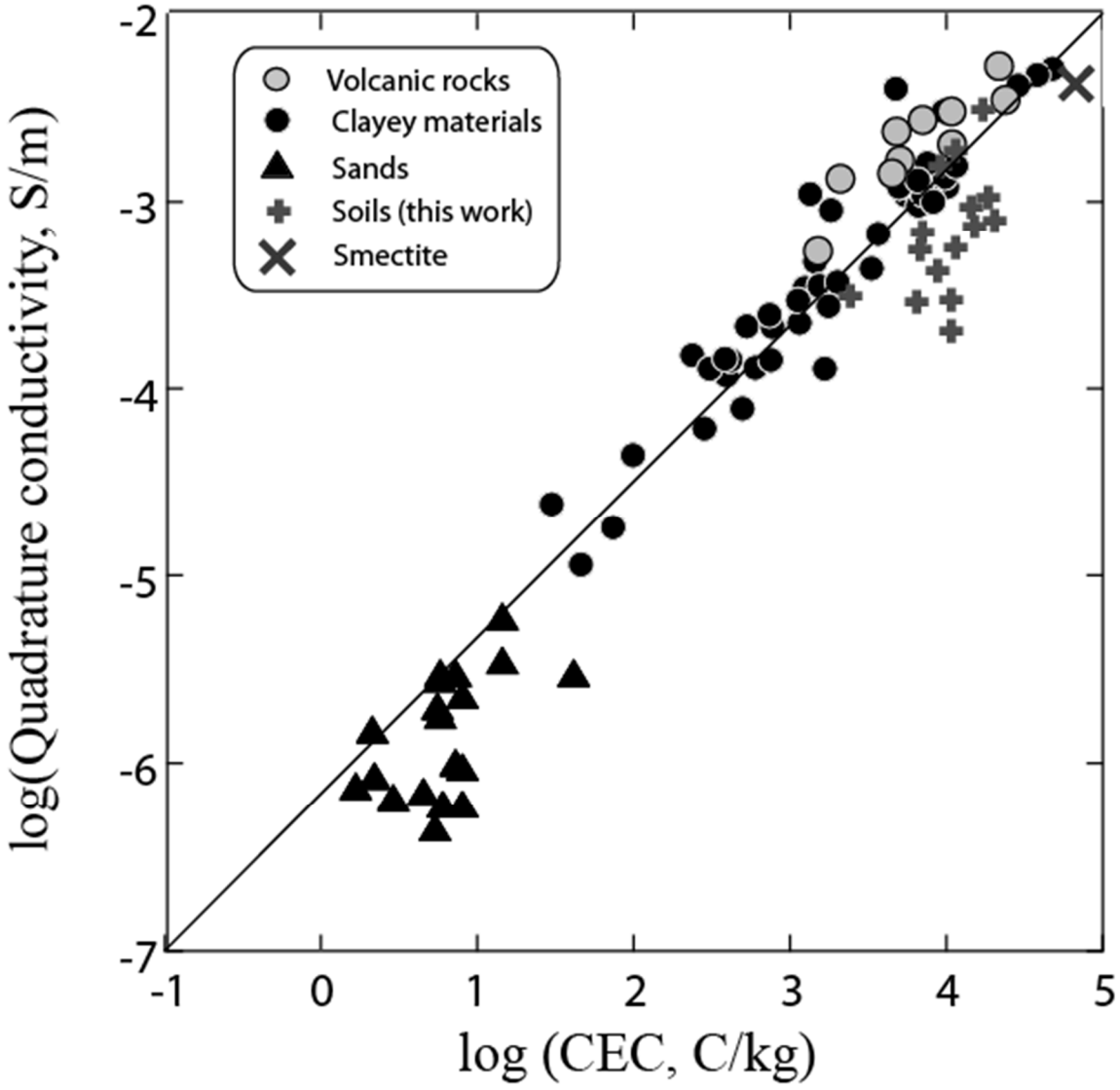

Figure 12. Quadrature conductivity (1 Hertz) versus cation exchange capacity (CEC, cobalthexamine method) for high porosity (>0.20, saturated) core samples. The data shown in the figure are Revil et al. (2017a, b, c) and Revil et al. (2018a). The overall trend confirms the linear dependence (r^2 = 0.91 in a log–log space) between the quadrature conductivity and the CEC for high porosity core samples. Note: 1 meq /(100 g) = 963.2 C kg^{-1}.

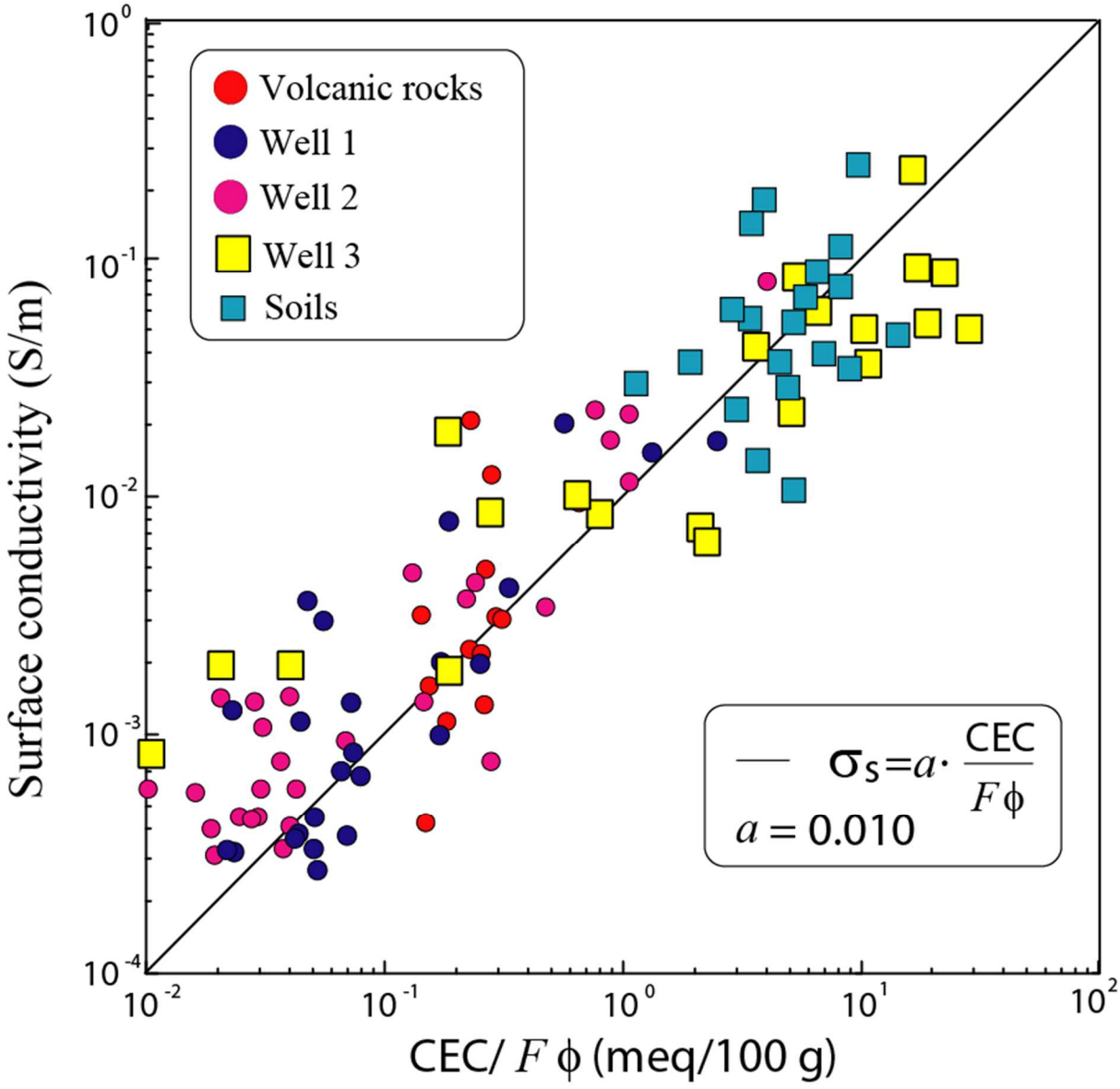

Figure 13. Surface conductivity versus normalized cation exchange capacity (CEC divided by the tortuosity, which is given by the product of the formation factor F by the porosity ϕ) for samples characterized by a broad range of porosity. The slope a is consistent with the theory presented in the main text for which $a = \rho_g B = 8.2\times10^{-6}$ kg $s^{-1}V^{-1}$= 0.008 S m^{-1} /(meq/100 g) close to the best fit value (0.010 S m^{-1} /(meq/100 g)). Note that here we are using siliciclastic materials, which explain the value of ρ_g. For carbonate-rich soils, the mass density of the grains is higher (ρ_g= 2800 kg m^{-3}). Data from Revil et al. (2021, volcanic rocks).

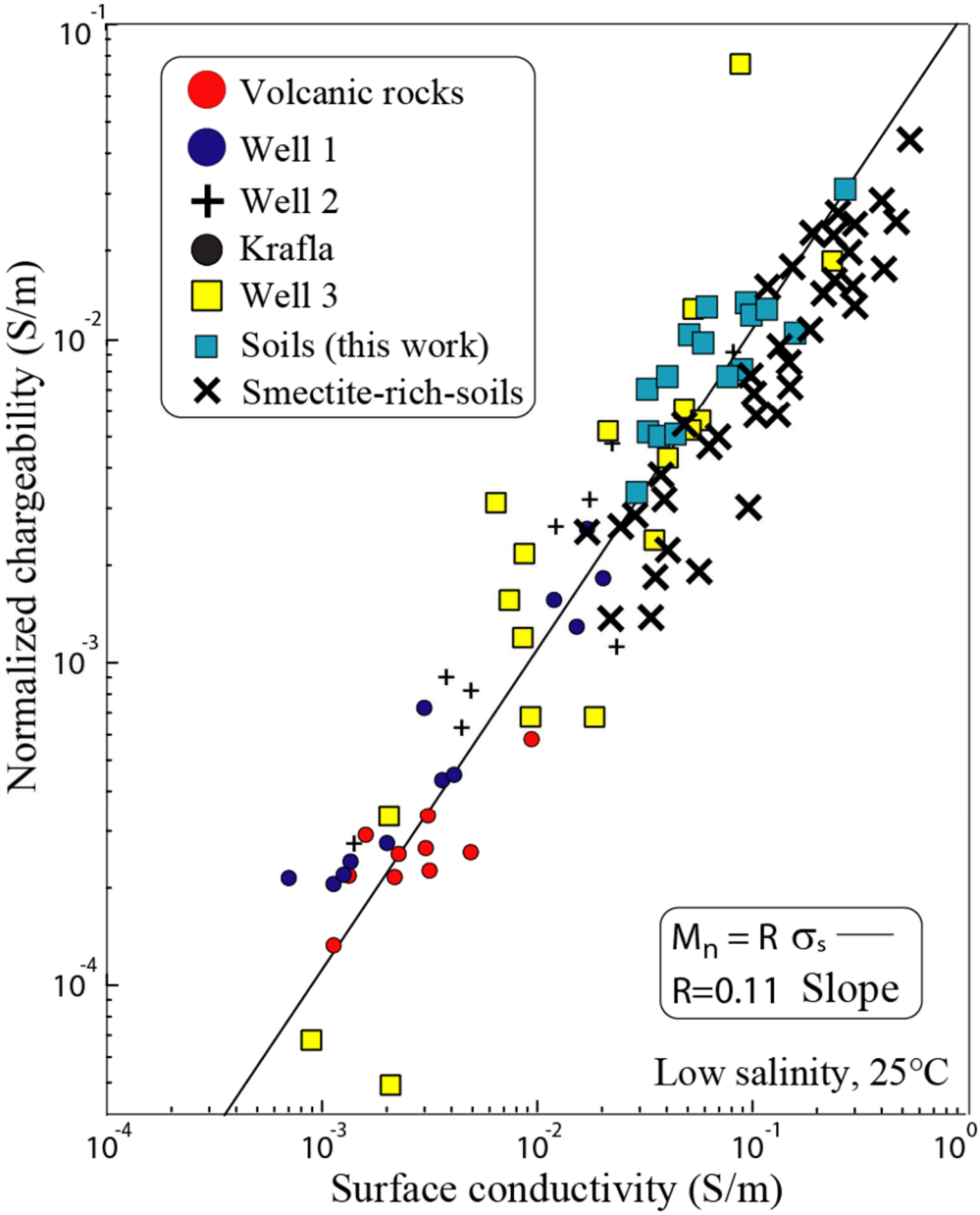

Figure 14. relationship between normalized chargeability and surface conductivity. Comparison between the soil samples of the present study, the smectite-rich soil samples from the study of Revil et al. (2017a) and volcanic rock samples (consolidated and not consolidated) from Hawaii and Krafla volcanoes (in Iceland, see Revil et al., 2018 and Ghorbani et al., 2018) excluding core samples with magnetite or pyrite. The slope of the trend provides the value of the funadamental dimensionless coefficient R, which is consistent with previous estimates of this parameter. Data from Revil et al. (2021, volcanic rocks) and Revil et al. (2017a, smectite-rich soils).

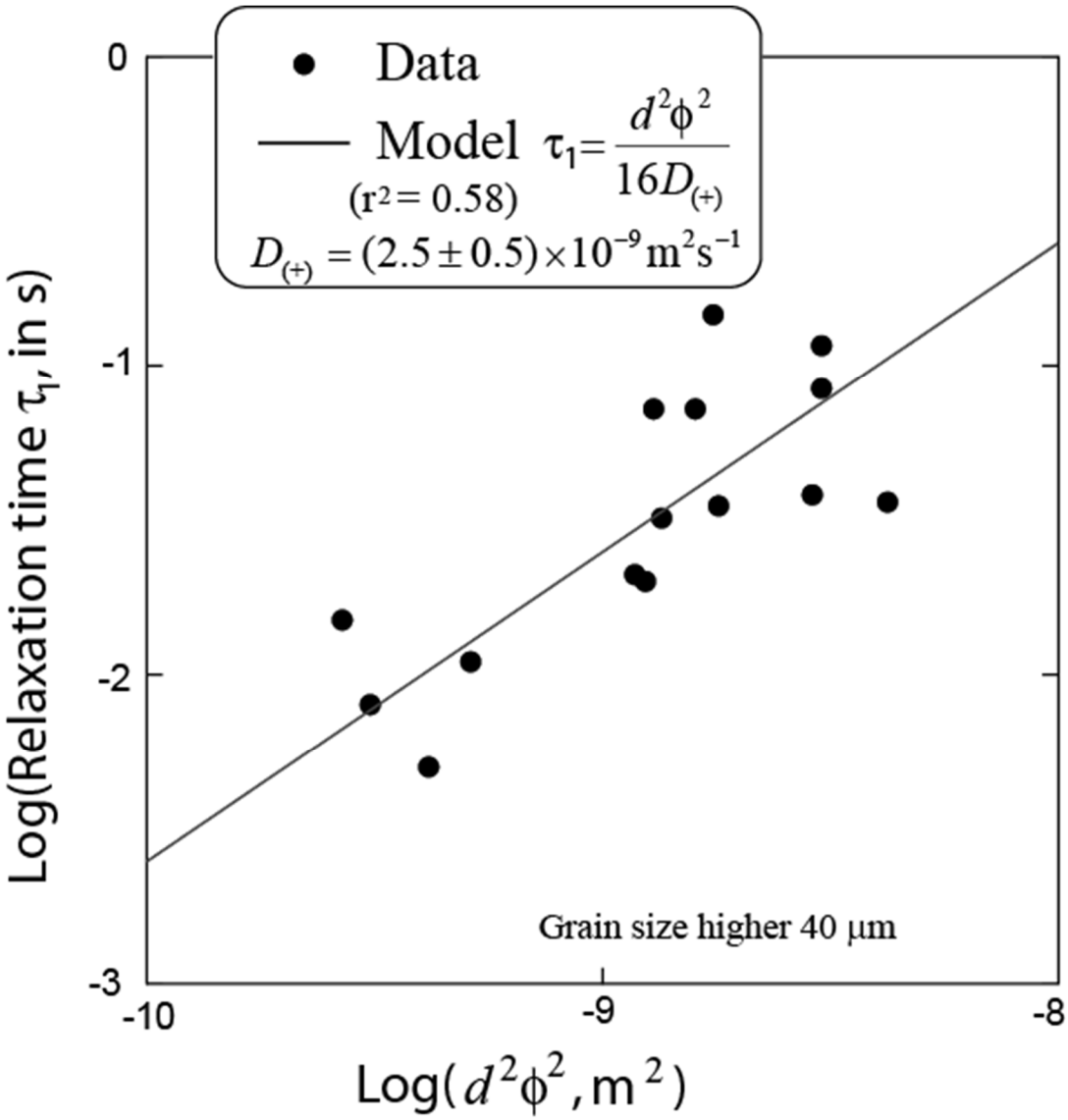

Figure 15. Relaxation time versus grain size (mean of the distribution above 40 μm) times the porosity for the sandy materials of the present study (saturated core samples). We use the relaxation time τ_1 corresponding to the coarse fraction of the material (see Table 2). The linear trend (r^2 = 0.58 in a log-log space) is used to compute the value of the diffusion coefficient $D_{(+)} = (2.5 \pm 0.5) \times 10^{-9}$ $m^2 s^{-1}$. Only the sandy cores (grain size higher than 40 μm have been considered here).

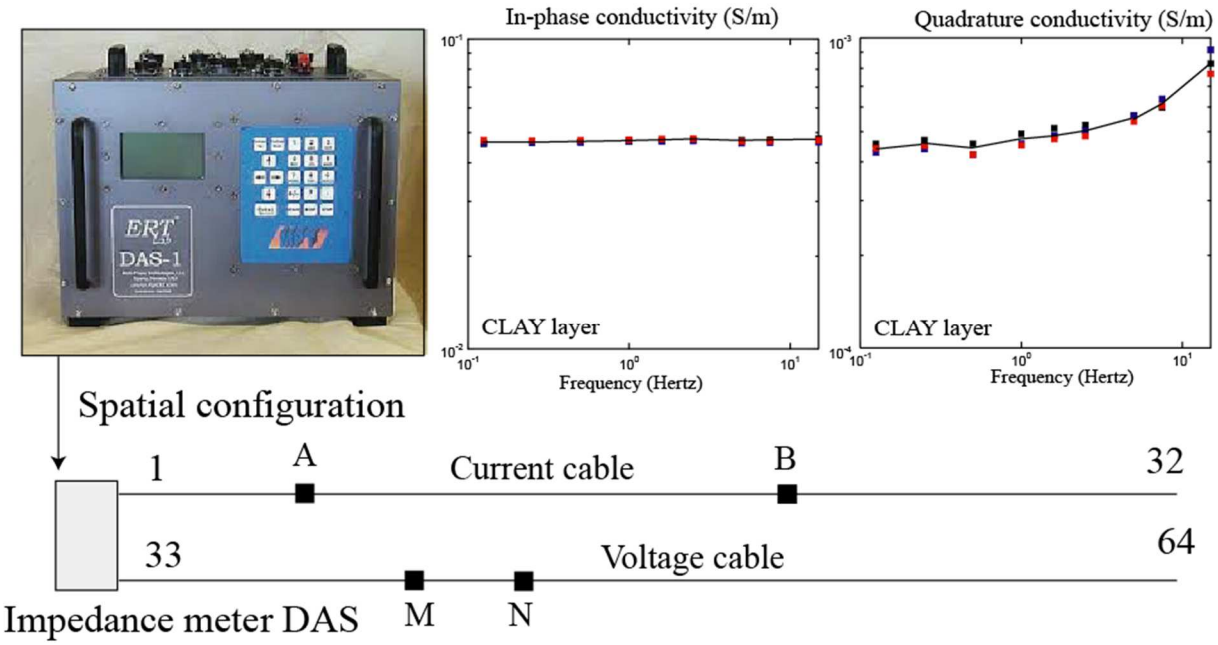

Figure 16. Setup of the field acquisition system. The current electrodes AB and the voltage electrodes MN are locates along separated cables to limit capacitive and inductive coupling effects. The acquisition was done with a Wenner-type configuration with a total of 64 electrodes. We use an impedance meter operating in the frequency-domain (DAS-1 from Multi-Phase Technologies, LLC). The figure displays also the complex conductivity spectra obtained in the field from this equipement at three locations corresponding to the clay layer.

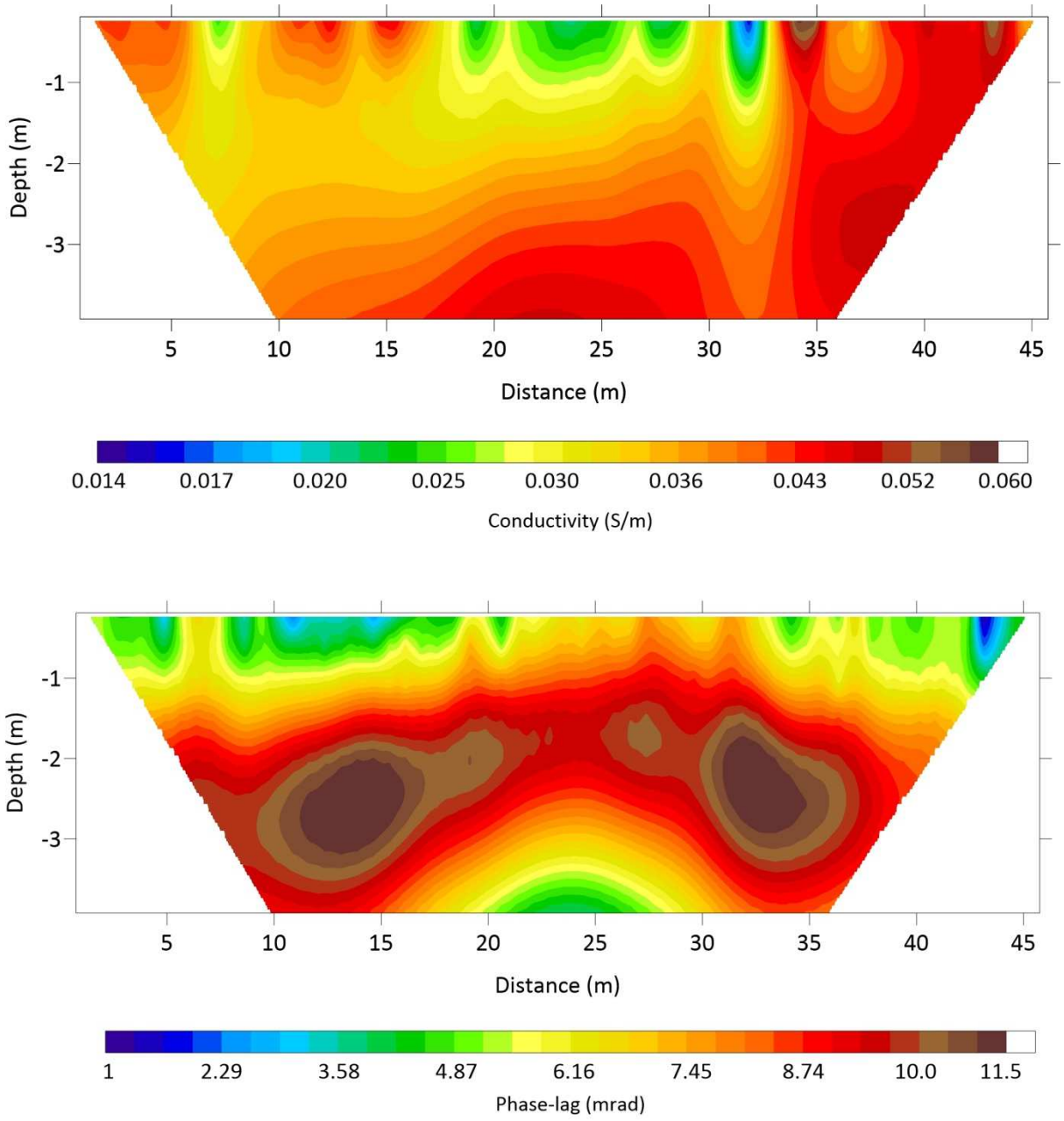

Figure 17. Conductivity and phase lag tomography for the geophysical profile shown in Figure 2 at 1 Hertz for the first 4 m below the ground surface. The conductivity profile does not display a lot of information while the phase exhibits a layer of high phase values (>9 mrad), possibly associated with a clay layer that has been recognized by drilling nearby.

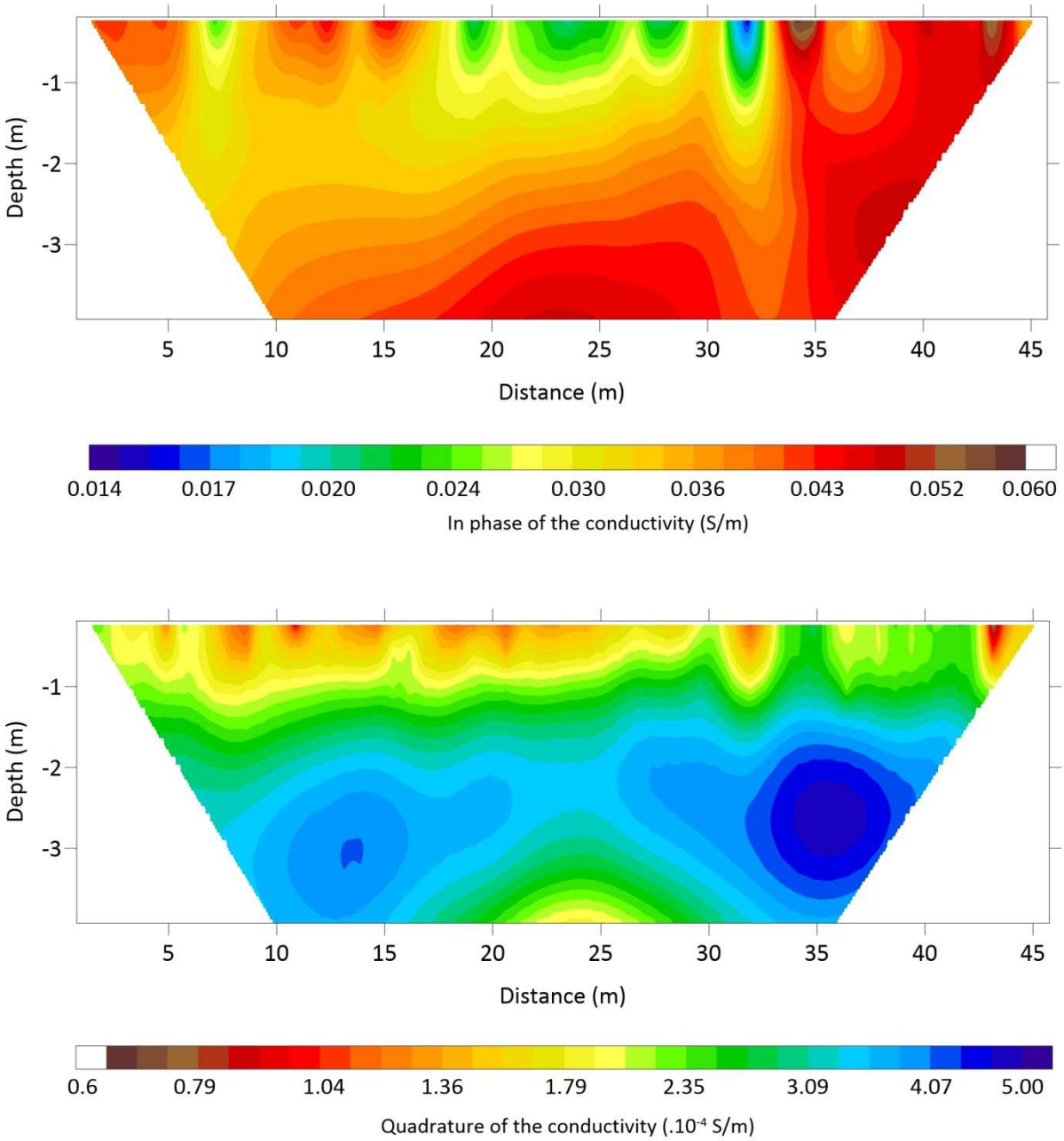

Figure 18. In phase and quadrature conductivity tomography for the geophysical profile P1 at 1 Hertz. The in-phase conductivity does not show clear structures while the quadrature conductivity tomogram displays a folded layer characterized by high values of the quadrature conductivity (> 3×10^{-4} S m^{-1}).

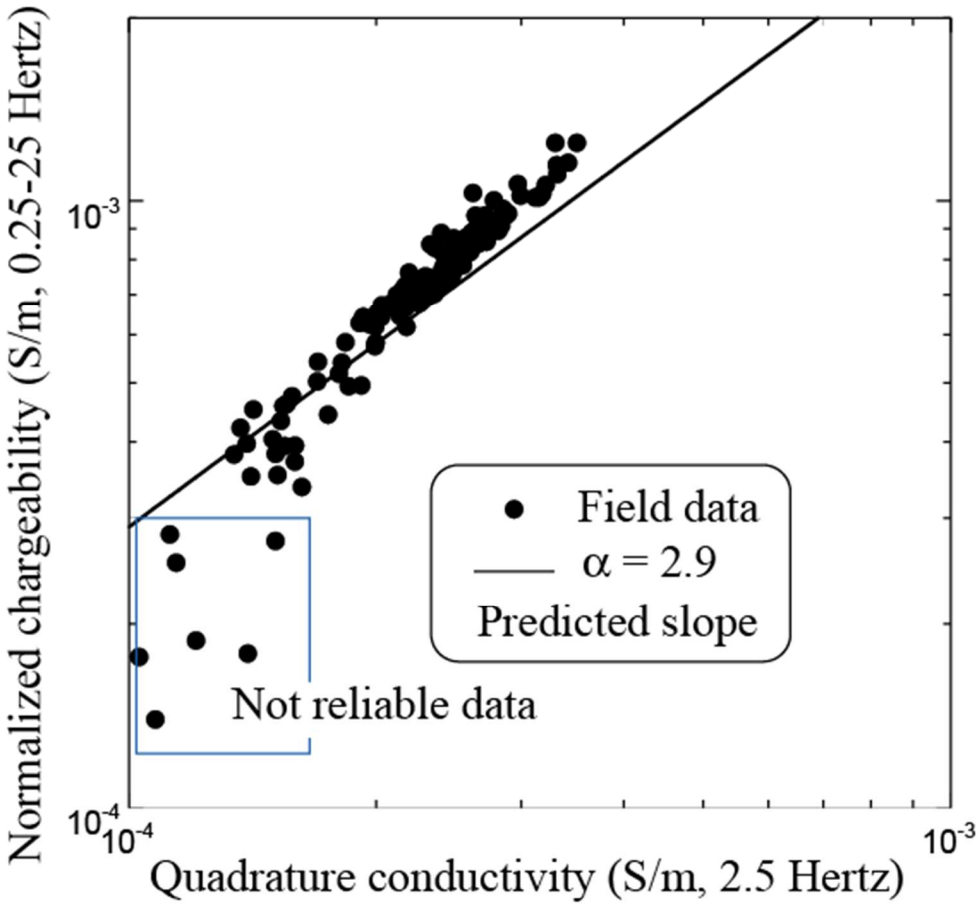

Figure 19. Normalized chargeability versus quadrature conductivity. The high and low frequencies (0.25 Hertz and 25 Hertz) are separated by 2 orders of magnitude, which yields a value of the slope equal to $\alpha = 2.9$ (from equation 9). Therefore the field data fairly agree with the model prediction (plain line) corresponding to equations (8) and (9). Please note that the plain line is therefore not a fit of the data in this plot. Low values in the quadrature conductivity are not reliable (see the outliers contained in the blue box).

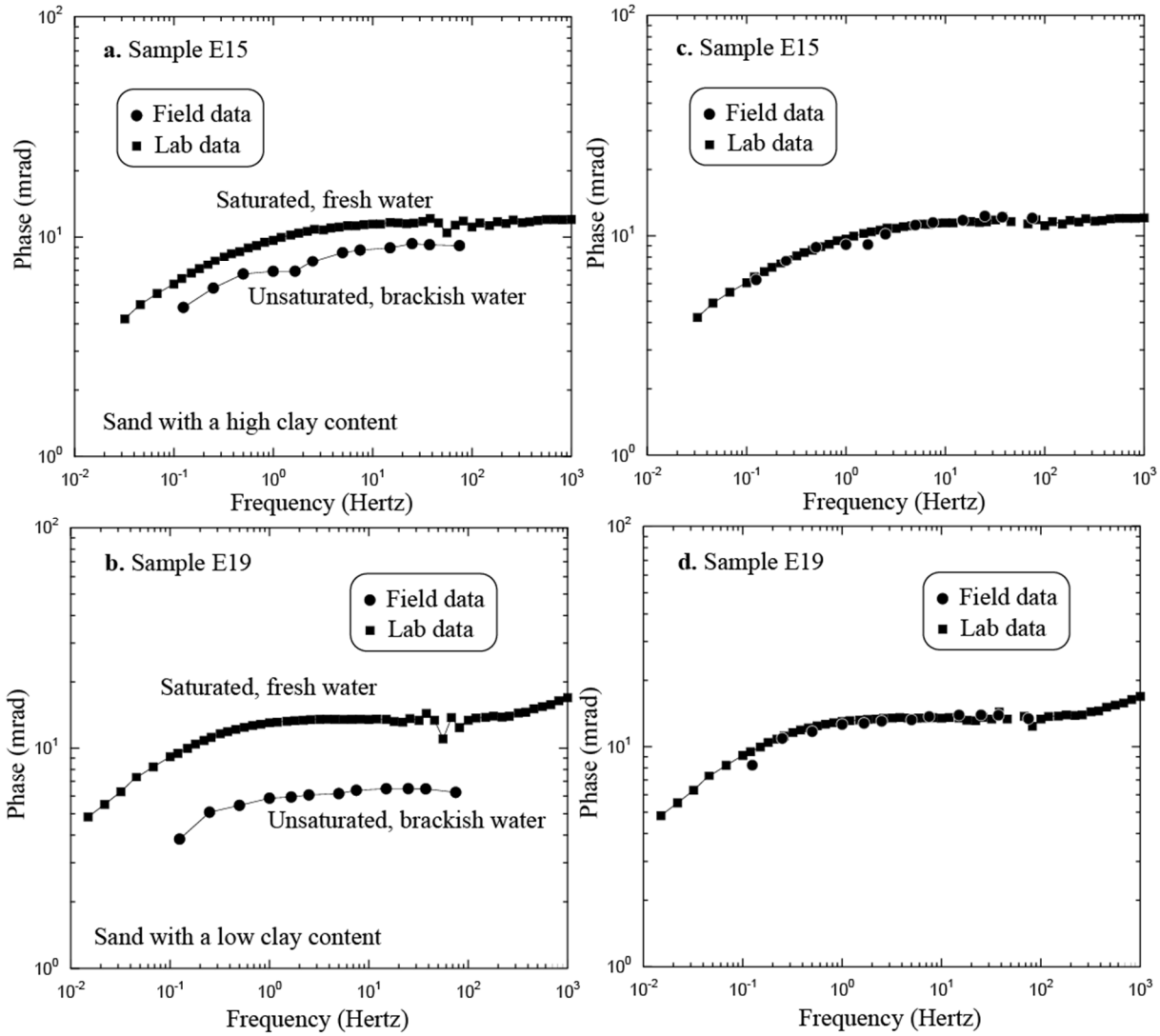

Figure 20. Comparison between the field and laboratory data. The field data are taken from the inverted tomograms at the position where the samples were extracted. The field data correspond to unsaturated conditions while the experimental data are taken at full saturation. **a.** Sample E15. **b.** Sample E19. **c.** Sample E15. Comparison of the phase spectra at saturation. **d.** Sample E19. Comparison of the phase spectra at saturation.

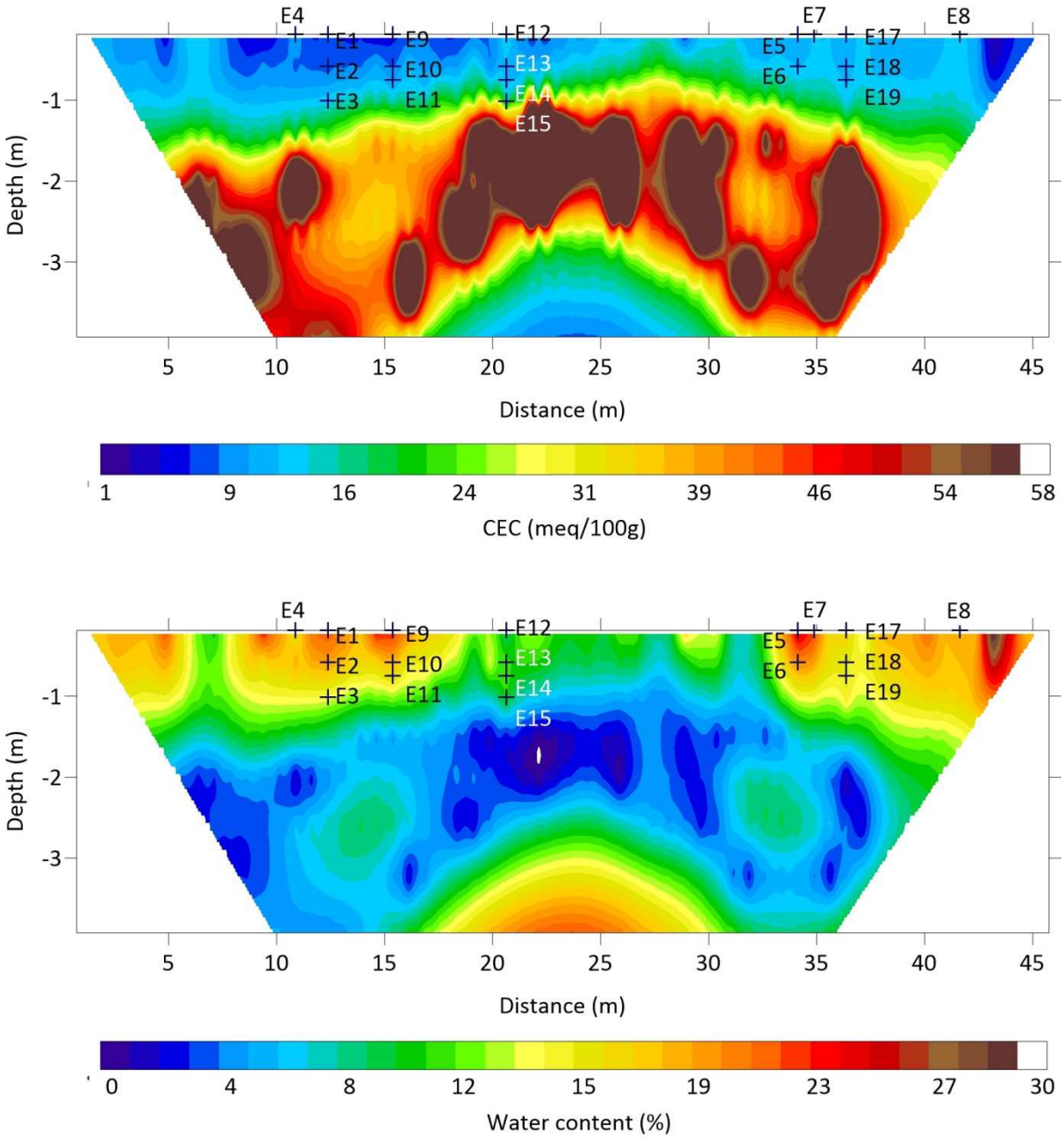

Figure 21. Tomography of the cation exchange capacity (CEC) and water content, θ, from the induced polarization tomography. From the tomogram, we observe a high-CEC low-water content dipping middle layer. Note that we use m = 1.7 for the full dataset but the true value of m in the clay formation is likely higher due to a higher CEC (see Revil et al., 1998, for an empirical trend between m and the CEC and the insert in Figure 14). A comparison between the CEC from the tomogram at the position of the core samples and the experimental data is given in Table 3.

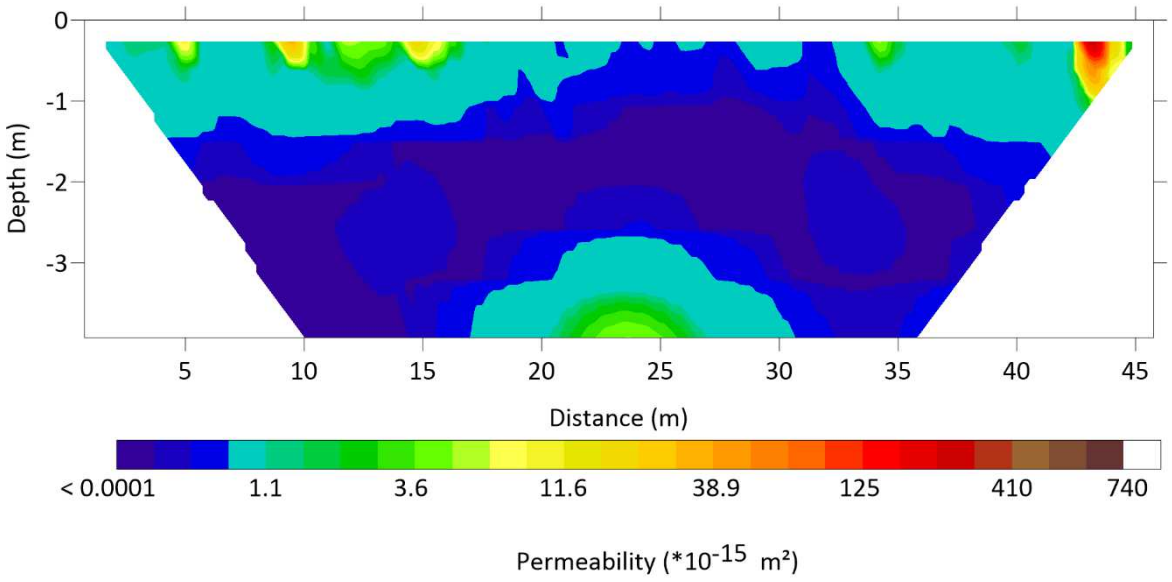

Figure 22. Soil permeability estimated from the data and spectral induced polarization tomography-based water content and cation exchange capacity (CEC) estimates. The estimation reveals that the middle layer is characterized by permeability values below 1 mD while the shallower (sandy) soils reach a permeability of 700 mD.

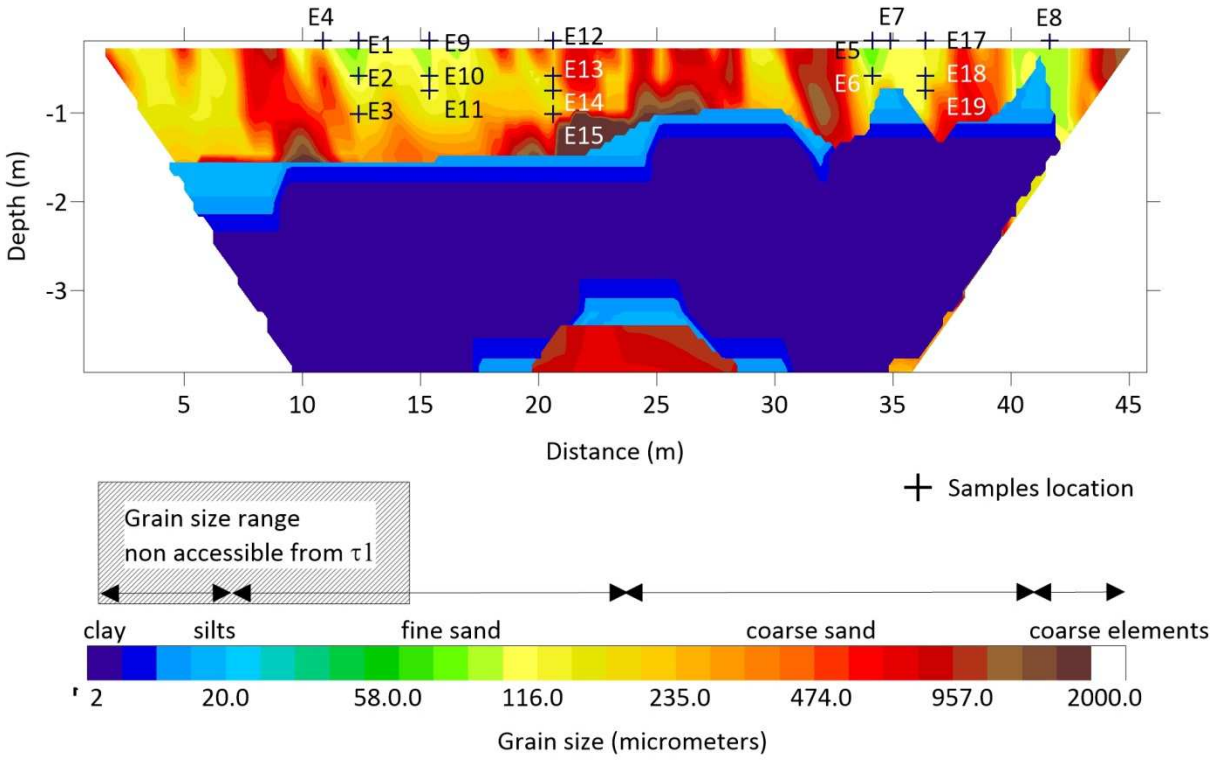

Figure 23. Tomography of the mean grain size from the relaxation time distribution determined from the spectra for each cell of the tomogram using a Cole Cole fit and the spectral induced polarization tomography-based water content values.

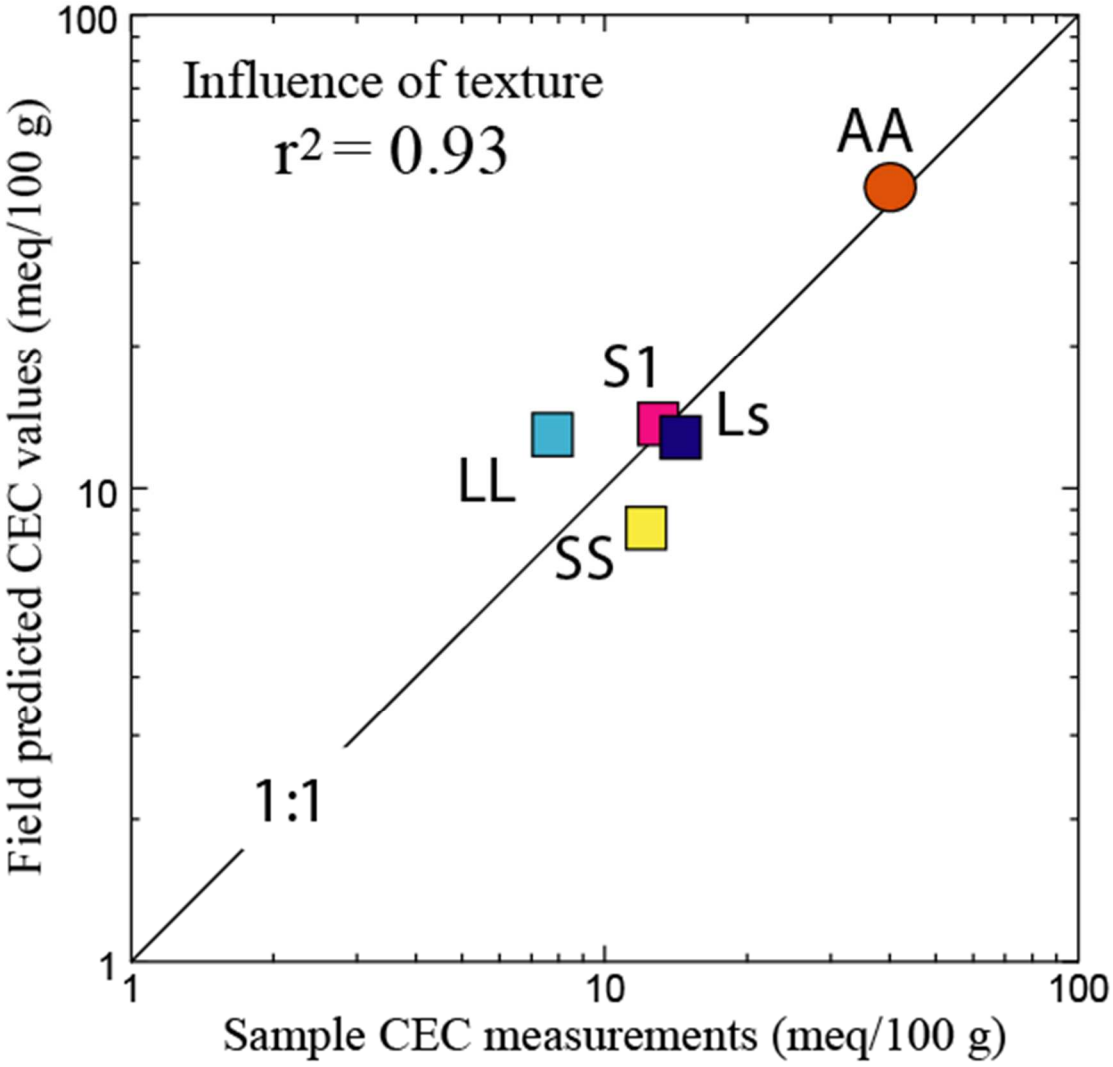

Figure 24. Field versus laboratory determination of the cation exchange capacity (in meq/100 g). The support volume of the laboratory core sample measurements is two orders of magnitude smaller than the support volume of the geophysical measurements. Therefore, we use here averaged values per texture type (SS: pure sand, Sl: silty sand, Ls: sandy silt, LL: pure silt, AA: clay end-member) for both the field and laboratory data to account for this point. The slope of the best least-square regression of a fit through (0,0) is 1.03. Forcing the fit to go through (0,0) is dictated by the underlying physics of the problem. The regression coefficient is given in a linear space.

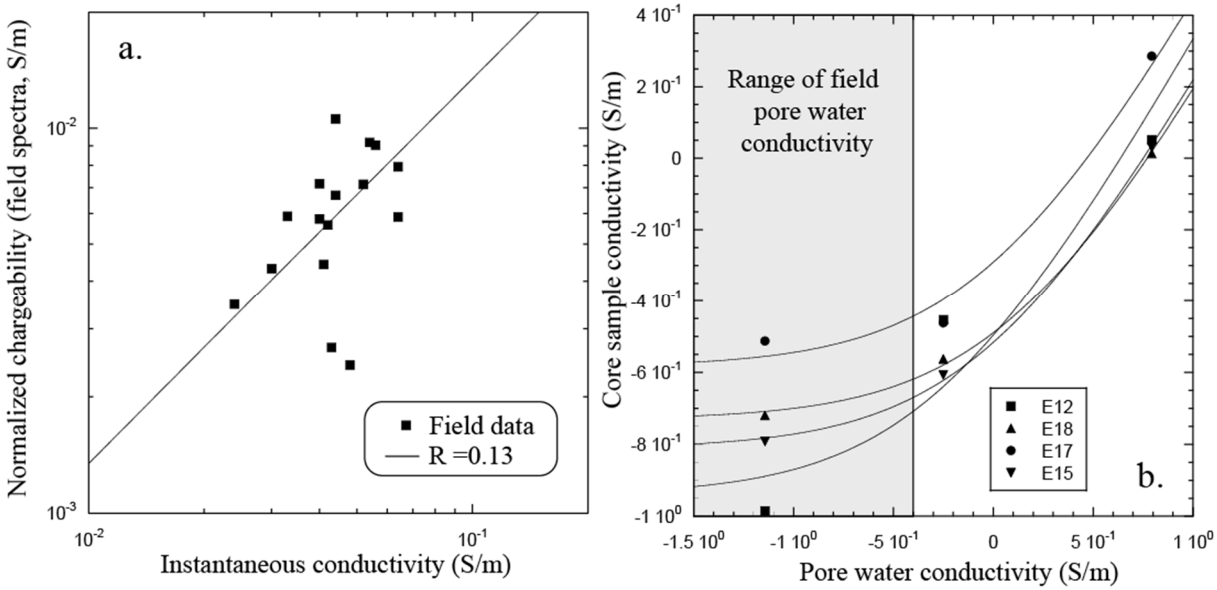

Figure 25. Importance of surface conductivity for the brine-saturated core samples. **a.** Normalized chargeability versus instantaneous conductivity (field data at the position of the core sample). The value of the slope indicates that surface conductivity dominates the conductivity response of the soils. **b.** Conductivity of the core sample versus the pore water conductivity in a log-log plot. In grey, we have plotted the range of the field pore water conductivity from fresh to brakish. For the full range, the data indicates that surface conductivity dominates the conductivity response of the material. R is indeed a constant independent of the relative importance of surface conduction. This is not the value of R that indicates if the surface conductivity dominates but the ratio between the normalized chargeability and the conductivity. This ratio is close to R if and only if surface conduction dominates.